Conformational Evolution of Molecular Signatures during Amyloidogenic Protein Aggregation.

George Devitt[a], William Rice[b], Anna Crisford[b,c], Iris Nandhakumar[b], Amrit Mudher[a]* and Sumeet Mahajan[b,c]*

a. Centre for Biological Sciences, University of Southampton, Highfield Campus, SO17 1BJ, Southampton, United Kingdom.

b. Department of Chemistry, University of Southampton, Highfield Campus, SO17 1BJ, Southampton, United Kingdom.

c. Institute for Life Sciences, University of Southampton, Highfield Campus, SO17 1BJ, Southampton, United Kingdom.

*s.mahajan@soton.ac.uk; a.mudher@soton.ac.uk

KEYWORDS. Alzheimer's disease, neurodegenerative diseases, amyloid, protein conformation, protein aggregation, Raman spectroscopy.

ABSTRACT: Aggregation is a pathological hallmark of proteinopathies such as Alzheimer's disease and results in the deposition of β-sheet-rich amyloidogenic protein aggregates. Such proteinopathies can be classified by the identity of one or more aggregated protein, with recent evidence also suggesting that distinct molecular conformers (strains) of the same protein can be observed in different diseases, as well is in sub-types of the same disease. Therefore, methods for the quantification of pathological changes in protein conformation are central to understanding and treating proteinopathies. In this work the evolution of Raman spectroscopic molecular signatures of three conformationally distinct proteins, Bovine Serum Albumin (α-helical-rich), β2-microglobulin (β-sheet-rich) and tau (natively disordered), was assessed during aggregation into oligomers and fibrils. The morphological evolution was tracked using Atomic Force Microscopy and corresponding conformational changes were assessed by their Raman signatures acquired in both wet and dried conditions. A deconvolution model was developed which allowed us to quantify the conformation of the non-regular protein tau, as well as for the oligomeric and fibrillar species of each of the proteins. Principle component analysis of the fingerprint region allowed further identification of the distinguishing spectral features and unsupervised distinction. While an increase in β-sheet is seen on aggregation, crucially, however, each protein also retains a significant proportion of its native monomeric structure after aggregation. Thus, spectral analysis of each aggregated species, oligomeric, as well as fibrillar, for each protein resulted in a unique and quantitative 'conformational fingerprint'. This approach allowed us to provide the first differential detection of both oligomers and fibrils of the three different amyloidogenic proteins, including tau, whose aggregates have never before been interrogated using spontaneous Raman spectroscopy. Quantitative 'conformational fingerprinting' by Raman spectroscopy thus demonstrates its huge potential and utility in understanding proteinopathic disease mechanisms and for providing strain-specific early diagnostic markers and targets for disease-modifying therapies.

INTRODUCTION

Proteinopathies are a group of diseases that are characterised by a conformational change in one or more proteins that causes a loss in physiological function and/or a toxic gain of function.[1] Such pathological changes in conformation typically result in the deposition of these proteins in β-sheet-rich deposits known as amyloid and are associated with disease progression. Hence, the detection and characterization of conformational changes is essential for both early diagnostic screening and the development of preventative therapeutic interventions.

Aggregation kinetics of amyloidogenic proteins have been intensely studied *in vitro*, with much interest in the structural changes that occur between the monomeric protein, it's misfolded state, as well as oligomeric and fibrillar conformations. In general, the characterisation of oligomeric species has been challenging due to a range of oligomeric species that may exist only transiently during the aggregation process,[2] but may also persist through the disaggregation of fibrillar species.[3] Examples of oligomeric diversity include fibrillar and non-fibrillar oligomers,[4] as well as toxic and non-toxic species.[5] A number of studies have demonstrated that oligomeric species are more toxic than fibrillar conformations both *in vitro*[3, 6] and *in vivo*[7-8]. The binding of conformationally dependant antibodies to a range of toxic protein oligomers suggests that toxicity is directly associated with protein conformation,[9] with toxic oligomeric species being rich in β-sheet secondary structure[6, 10] and displaying an increase in hydrophobic residue exposure.[11-13] Therefore, early aggregation species may represent valuable biomarkers for predictive disease diagnosis, as well as targets for disease-modifying treatment, underlining the requirement for further structural characterisation of amyloid oligomers.

A range of techniques have been used to probe the structure of amyloidogenic protein species including electron microscopy (EM), atomic force microscopy (AFM), X-ray diffraction (XRD), nuclear magnetic resonance (NMR), circular dichroism (CD), Fourier transform infrared spectroscopy (FTIR) and Raman spectroscopy. Vibrational spectroscopic techniques including FTIR and Raman have been widely applied to the study of protein conformation in the context of amyloid fibrils and neurodegenerative disease,[14] with much promise of future diagnostic application.[15] An increase in β-sheet is considered a hallmark of amyloid-directed aggregation and

is most commonly probed in biological studies *in vitro* using fluorescent dyes that bind to β-sheet, such as Thioflavin T (ThT). Furthermore, much work *in cellulo* makes use of the proximity of tagged chromophores by Förster Resonance energy transfer (FRET) to measure aggregation. However, such techniques give little insight into the conformation of proteins or their aggregates and are not quantitative enough to lend themselves to accurate structural discrimination or diagnosis.

Raman spectroscopy is a label-free optical technique that probes the vibrations of chemical bonds. Unlike infrared spectroscopy it is ideally suited to investigate aqueous matrices such as biofluids and biological systems *in situ* due to non-interference by water. It is non-invasive and non-destructive and can be directly used to provide chemical-structural information without, or with minimal, sample preparation. Biomedical samples, such as blood plasma,[16] can be fully- or partially-dried (as condensed droplets), in order to increase local concentration, allowing rapid spectral acquisition.[17-18] The resulting Raman spectrum provides a unique chemical fingerprint of the sample depending on its bond composition and molecular structure, making Raman spectroscopy a highly chemically selective technique. The Raman spectrum for proteins includes protein modifications such as metal binding and post-translational changes,[19-22] as well as secondary and tertiary structural information and can therefore provide a 'conformational fingerprint'. Conformational fingerprinting of toxic protein species can consequently reveal important links between protein structure and toxicity, as well as provide valuable spectral biomarkers for disease diagnosis.

Raman spectroscopy has been used previously to characterise different conformations of monomeric α-synuclein and it was shown that the technique was able to detect short stretches of secondary structure that were not detected using circular dichroism[23]. There is also evidence for variations in the chemical fingerprints of amyloid fibrils with parallel in-register β-sheet and β-solenoid conformations.[24] Raman spectroscopy has also been shown to distinguish differences in secondary structure between monomeric, oligomeric and fibrillar species for a range of species including α-synuclein,[25] prion protein,[26] human serum albumin[27] and amyloid β.[28] Furthermore, variations in β-sheet content and side chain interactions of fibrils formed from four disease-related α-synuclein mutants were characterised using Raman spectroscopy.[29] Together, these studies demonstrate the discriminative power of Raman spectroscopy for the analysis of protein conformers.

In this study we have used the structurally diagnostic nature of Raman spectroscopy to compare changes in conformation of three differently structured proteins on aggregation. In particular, we wanted to develop a methodology by which conformational changes in a natively disordered (unstructured or non-regular structured) protein could be understood by learning from the analysis of proteins with stable secondary structural elements such as α-helices and β-sheets. We chose to do this with three proteins: the α-helical protein bovine serum albumin (BSA), the β-sheet protein β2-microglobulin (β2M), implicated in dialysis related amyloidosis, and the intrinsically disordered protein tau (implicated in tauopathies such as Alzheimer's disease), because although all of them form fibrillar aggregates they have intrinsically different conformations. Starting with three proteins with distinctly different conformations allowed insight into evolution of their secondary structures on aggregation into oligomeric and fibrillar species. Morpho-chemical analysis of the aggregation species (monomer, oligomer and fibril) s carried out by atomic force microscopy (AFM), structurally-sensitive fluorescent dyes and Raman spectroscopy. We present Raman spectra from both proteins in the solution-state (wet) and completely dried by drop-deposition. This enables us to evaluate how the drying process affects protein structure and therefore the utility of drop-deposition Raman spectroscopy (DDRS) for classification of protein species, which is important for many biomedical applications including diagnostic methods. It has been demonstrated previously that proteins remain partially hydrated upon drop-deposition and largely retain their secondary structure.[17-18] Our data demonstrates that as each protein aggregates, there is an evolution of the conformation towards a predominantly β-sheet structure, regardless of the original conformation of the monomeric protein. Nevertheless, each species has a unique and quantitative 'conformational fingerprint'. We deconvolved the structural information from the conformationally sensitive Amide I peak and crucially, combining this with information from the published crystal structures for monomeric bovine serum albumin and β-2 microglobulin, allowed us to quantify the conformation of the non-regular protein tau, as well as the oligomeric and fibrillar species of each protein. We further show through unsupervised principal component analysis that each of the species for each protein as well as oligomers and fibrils from different proteins are distinctly classified. Despite some expected changes in protein conformation upon drying, we show that each protein species can be distinguished and well-classified based on its secondary structure in both the concentrated solution-state and the fully dried solid-state, validating that the latter approach as suitable for potential diagnostic purposes. Our work also demonstrates that Raman spectroscopy can be used to ascribe a unique "conformational fingerprint" for distinct protein conformers (even if they are intrinsically disordered), whether they are monomers, oligomers or fibrils. This offers a direct, label-free method for the identification and targeting of distinct protein conformers, which can pave the way for novel strain-specific early diagnostic markers and disease-modifying therapies.

RESULTS

In vitro aggregation assays were used to induce aggregation of three different proteins, each with an intrinsically different monomeric conformation, and the evolving aggregated species were characterized with AFM, Thioflavin T (ThT) fluorescence, 4,4′-Dianilino-1,1′-binaphthyl-5,5′-disulfonic acid dipotassium salt (Bis-ANS) fluorescence and Raman spectroscopy. A schematic of the workflow is shown in figure 1. The aggregation was set up and tracked by ThT and Bis-ANS fluorescence and AFM to observe and confirm the formation of oligomers and fibrils. ThT and Bis-ANS bind to β-sheet and hydrophobic structure respectively, whilst AFM provides morphological detail at nanoscale resolution. For each protein, the monomeric species at the start of the experiment, as well as the intermediate oligomeric species and fibrils observed towards the end of the aggregation process, were analysed by Raman spectroscopy. Raman spectroscopy was performed both on the solution-state and on dried samples. Both the Amide I (1600 -1700 cm^{-1}) and Amide III (1200 – 1300 cm^{-1}) regions of the Raman spectrum of proteins are used as a marker of secondary structure. However, Amide III analysis is somewhat more complex than Amide I in that it is the product of equal contributions of C-N stretching and N-H bending vibrations with some contribution from C-C stretching.[30] Typically, α-helical structures have weak Amide III signals, but can be observed in the broad range of 1250 – 1300 cm^{-1}. β-sheet structures give a strong peak at lower frequencies, 1220 - 1248 cm^{-1} while nonregular and turn structures are typically observed at 1245 - 1270 cm^{-1}.[31-32] On the other hand, the Amide I peak of the protein Raman spectrum corresponds to the stretching vibration of C = O and is most widely used for the analysis of secondary structure.[31, 33] Hence, in this work, Amide I peaks were analysed in detail by carrying out spectral deconvolution to understand the changes

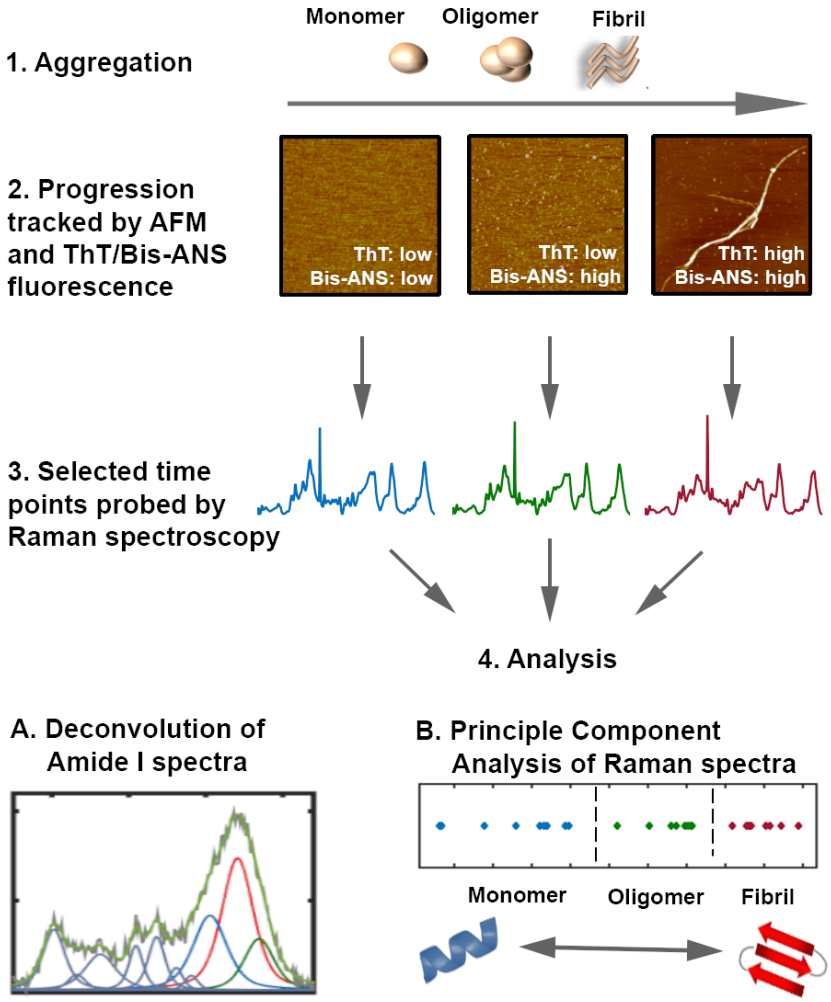

Figure 1 - Schematic of workflow. 1. Proteins were aggregated in conditions to form oligomeric and fibrillar species. 2. Atomic Force Microscopy (AFM), Thioflavin T (ThT) fluorescence and Bis-ANS fluorescence was used to track and confirm protein aggregation before Raman analysis. 3. Samples were probed by Raman spectroscopy in wet conditions, and after drying by drop-deposition. 4. Raman spectra were analysed in two ways: A. The Amide I region was deconvolved using mixed Gaussian/Lorentzian curves at starting frequencies identified from second derivative spectra in order to determine the secondary structural content of each protein. B. Principle Component Analysis (PCA) was applied to all acquired spectra in order to classify data and to identify regions of spectral variation between datasets.

in the secondary structure of all proteins and their aggregated species. Based on experiment and calculations, Amide I frequencies for different secondary structures are assigned as follows: 1650 – 1658 cm^{-1} (α-helix), 1668 – 1674 cm^{-1} (β-sheet), 1660 – 1667 cm^{-1} and 1674 – 1689 cm^{-1} (nonregular).[31, 34-38]. A lack of detectable protein structure can be defined as unordered, disordered or random, but these terms may not be accurate, as the protein may still contain segments of ordered structure or structures that are not well defined. Therefore, we choose to use the term 'nonregular' to define such structure. As proteins are made up of a mixture of secondary structural elements, the Amide I peak represents the sum of these elements, each of which has a discrete vibrational frequency. Therefore, deconvolution of the Amide I peak provides a quantitative estimation of secondary structure content. The Amide I region including 1525 cm^{-1} – 1725 cm^{-1} was deconvolved using an established method[23, 32] comprising of 3 mixed Gaussian/Lorentz curves representing secondary structural components (described as peaks 1-3 in the text), as well as a curve ~1635 cm^{-1} that may represent nonregular structure and/or its vibrational coupling to other secondary structures,[39] and curves representing aromatic amino acids including tryptophan, phenylalanine and tyrosine; ~1550 cm^{-1} and ~1580 cm^{-1}, ~1605 cm^{-1}, ~1615 cm^{-1}, respectively. The fitting parameters were designed based on previous literature and taking into account the crystal structures of BSA and β2M. The starting frequency for each peak was determined by taking the second derivative of the Amide I region.[40] The same parameters were then applied to the Amide I spectra of tau and aggregated species of all proteins. The results and analysis are detailed for each protein below.

Bovine Serum Albumin (BSA)

BSA is a protein derived from the blood serum of cows that functions as a shuttle for many biological and chemical substrates, as well as maintaining the pH and osmotic pressure of the blood.[41] The formation of BSA fibrils has not been reported *in vivo*, but extremes of pH and temperature have been shown to induce aggregation *in*

vitro.[42-44] For aggregation, BSA was dissolved in water (pH 3) at a concentration of 60 mg/ml and heated to 65°C. The formation of fibrils was tracked using AFM (figure 2A-C). Aggregation occurred rapidly, which is expected as BSA aggregation is not dependant on nucleation meaning that there is no lag phase.[45] Oligomeric aggregates with spheroidal morphology as observed by AFM were formed after 5 minutes of incubation and the aggregation process was complete by 24 hours, which produced fibrils with a short and curly morphology Height profiles for AFM images of each BSA aggregation species are shown in supplementary figure 1 which indicate that BSA oligomers have an average height ~3-4 nm and BSA fibrils have an average height of ~5-6 nm

Solution samples were combined with ThT or Bis-ANS dye in order to assess protein folding. ThT fluorescence intensity was increased upon oligomerisation, and strongly increased upon the formation of fibrils (figure 2D), suggesting the formation of cross- β architecture. Concurrently, Bis-ANS fluorescence intensity was increased upon oligomerisation and remained similarly intense upon the formation of fibrils (figure 2E), suggesting an increase in hydrophobicity upon oligomerisation.

Raman spectroscopy was performed at the same time points. Raman spectra were acquired in wet and in dried conditions. Small volumes of each sample (0.5µl) were spotted onto quartz coverslips to create a concentrated droplet or and then further dried in a vacuum to create the dried samples. The method of analysis is referred to as drop-deposition Raman spectroscopy (DDRS)17,18 The Amide I second derivative spectra of each aggregation species in wet conditions is shown in figure 2F. The secondary structural components for the monomer are labelled. These spectra highlight the change in peak frequency during BSA aggregation, most notably the shift in ratio between the peak ~1655 cm^{-1} and the peak ~1670 cm^{-1} during the formation of oligomeric and fibrillar species, suggesting the formation of β-sheet secondary structure. There are slight differences observed between the Amide I spectra measured in wet and dried conditions for each species (Figures G-I). An increase in the higher frequency region of the Amide I spectra >1660 cm^{-1} indicates an increase in nonregular and/or β-structure upon drying, with little or no change in the frequency of Amide I maxima. As expected the least difference is observed between the spectra for fibrils.

For quantitative secondary structural analysis deconvolution of the Amide I spectral region was carried on both, spectra acquired under wet and dried conditions. The crystal structure of BSA shows that the protein contains primarily α-helical secondary structure (74%) with no detectable β-sheet content.[46] The Amide I peak of the BSA monomer is observed at 1654/1655 cm^{-1} (wet/dried) in the Raman spectrum (Figure 2G), with no distinct peak in the Amide III region (supplementary figure 2B). Deconvolution of the Amide I peak enabled the calculation of secondary structural content. Fitted curve frequencies and secondary structural assignments are summarised in table 1, and curve fitted spectra are shown in supplementary figure 3. For the wet monomer, the peak observed at 1655 cm^{-1} (curve 1) comprises 73% of the secondary structural content and is assigned to α-helical structure, in good agreement with the crystal structure for BSA. Peak 2 is observed at 1675 cm^{-1} and accounts for 24% of the secondary structural content. It has been noted that nonregular structure may be difficult to distinguish from β-sheet structures based on Raman frequency alone.[31] However, no β-sheet is observed in the BSA crystal structure and peak 2 has a higher frequency than that typically seen for Raman β-sheet vibrations, suggesting that peak 2 is a nonregular component.[23, 32, 47-48] Peak 3 makes up 3% of the secondary structural content of BSA and is centred at 1687 cm^{-1}. This peak can also be assigned to nonregular and turn structure.[23, 32, 38, 49]

Table 1. Results from Amide I peak deconvolution in wet and dry conditions

Protein	Wet			Dried		
	Peak Frequency (cm^{-1})	Peak Area (%)	Peak Assignment	Peak Frequency (cm^{-1})	Peak Area (%)	Peak Assignment
BSA monomer	1655	73	α-helix	1655	57	α-helix
	1675	24	Nonregular	1667	19	Nonregular
	1687	3	Nonregular	1683	24	Nonregular
BSA oligomer	1653	63	α-helix	1656	53	α-helix
	1671	31	β-sheet	1670	26	β-sheet
	1686	6	Nonregular	1685	21	Nonregular
BSA fibril	1654	45	α-helix	1656	44	α-helix
	1670	37	β-sheet	1670	32	β-sheet
	1685	18	Nonregular	1685	24	Nonregular
β2M monomer	1654	33	Turn	1655	35	Turn
	1671	52	β-sheet	1670	42	β-sheet
	1685	15	Nonregular	1684	23	Nonregular
β2M oligomer	1659	48	Turn	1659	48	Turn
	1672	27	β-sheet	1671	33	β-sheet
	1685	25	Nonregular	1684	19	Nonregular
β2M fibril	1660	37	Turn	1661	33	Turn
	1673	60	β-sheet	1674	66	β-sheet
	1689	3	Nonregular	1689	1	Nonregular
Tau monomer	1663	59	Nonregular	1655	38	α-helix/turn
	1674	2	Nonregular	1671	31	β-sheet
	1683	39	Nonregular	1687	31	Nonregular
Tau oligomer	1657	38	α-helix/turn	1654	41	α-helix/turn
	1670	23	β-sheet	1670	36	β-sheet
	1683	39	Nonregular	1686	23	Nonregular
Tau fibril	1650	41	α-helix/turn	1656	35	α-helix/turn
	1671	49	β-sheet	1671	42	β-sheet
	1688	10	Nonregular	1686	23	Nonregular

Values determined from Amide I deconvolution (supplementary figures 3 and 4)

Deconvolution of the Amide I band of the wet oligomer shows a reduction in the area of curve 1 from 73% - 63%, suggesting a loss of α-helical structure. Furthermore, peak 2 shows a shift in frequency from 1675 cm^{-1} to 1670 cm^{-1}, suggesting that the oligomer has adopted β-sheet structure that makes up 31% of secondary structural content. The BSA fibril shows a further loss in α-helical structure (63% - 45%) and a further increase in β-sheet structure (31% – 37%), which is similar to previously published results using FTIR.[43] The loss in α-helical structure and gain in β-sheet structure during aggregation can also be observed by a decrease in the backbone/skeletal peak at 942 cm^{-1} (C – C backbone stretch) and in increase in the Amide III peak at 1238 cm^{-1}, respectively (supplementary figure 2).

The dried monomer spectrum reveals a decrease in peak 1 area (73% - 57%) in comparison to the monomer in wet samples, corresponding to a loss in α-helical structure upon drying. A shift in peak 2 frequency from 1675 cm^{-1} to 1667 cm^{-1} is also observed, suggesting that this curve is sensitive to hydration and/or aggregation has occurred. This curve sits at a lower frequency than observed for amyloidogenic β-sheet structure in BSA (1670 – 1671 cm^{-1}) and is therefore assigned to non-hydrated, nonregular structure. Similarly, peak 3 lowers in frequency upon drying from 1687 cm^{-1} – 1683 cm^{-1}, as well as increasing in area from 3% - 24%, highlighting an increase in nonregular structure in monomeric dried BSA. On analysis of each of the samples after drying, a decrease in α-helical structure upon oligomerisation (57% - 53%) and upon fibril formation (44%) is observed which occur concomitantly with increases in β-sheet structure area from monomer (1667 cm^{-1}, 19%) to oligomer (1670 cm^{-1}, 26%) and finally fibril (1670 cm^{-1}, 32%). Thus the structural evolution during aggregation shows a similar pattern on analysis of dried samples as compared to analysis under wet conditions.

After the quantification of BSA secondary structure, principle component analysis (PCA) was applied separately to the spectra acquired in wet and dry conditions in order to classify the spectra using a non-biased method. The PCA scores plot revealed that only one principle component (PC1) was required for the separation of the BSA aggregation species for spectra acquired under wet (figure 3A) and dried (figure 3C) conditions. The PCA loadings plot shows the coefficient of variance that correlates each principal component to the original variables, that is, the recorded frequencies in Raman spectra (figure 3B,D). Therefore, these loadings show the regions in the spectra that explain the highest variation within the dataset,

meaning that these changes directly represent changes in bond/structural composition during aggregation.

High variation is observed in the Amide I, Amide III and skeletal region of the loadings spectrum for wet BSA species. A comprehensive list of loadings peaks for each protein is tabulated in supplementary table 1. Peaks representing α-helical structure; 1652 cm^{-1} (Amide I), 1307 cm^{-1} (Amide III)[50] and 943 cm^{-1} (skeletal)[51] have a negative coefficient on the loadings plot for PC1, and peaks representing β-sheet structure; 1672 cm^{-1} (Amide I), 1237 cm^{-1} (Amide III) have a positive coefficient. This is reflected in the scores plot, which shows that monomeric BSA spectra have a negative PC1 score (< -1), oligomeric spectra have a less-negative score (> -1) and fibrillar BSA spectra with positive PC1 scores (> 1), highlighting a gain in β-sheet secondary structure and a loss of α-helical structure during aggregation. Peaks in the skeletal region corresponding to β-sheet structure are poorly characterised, but a

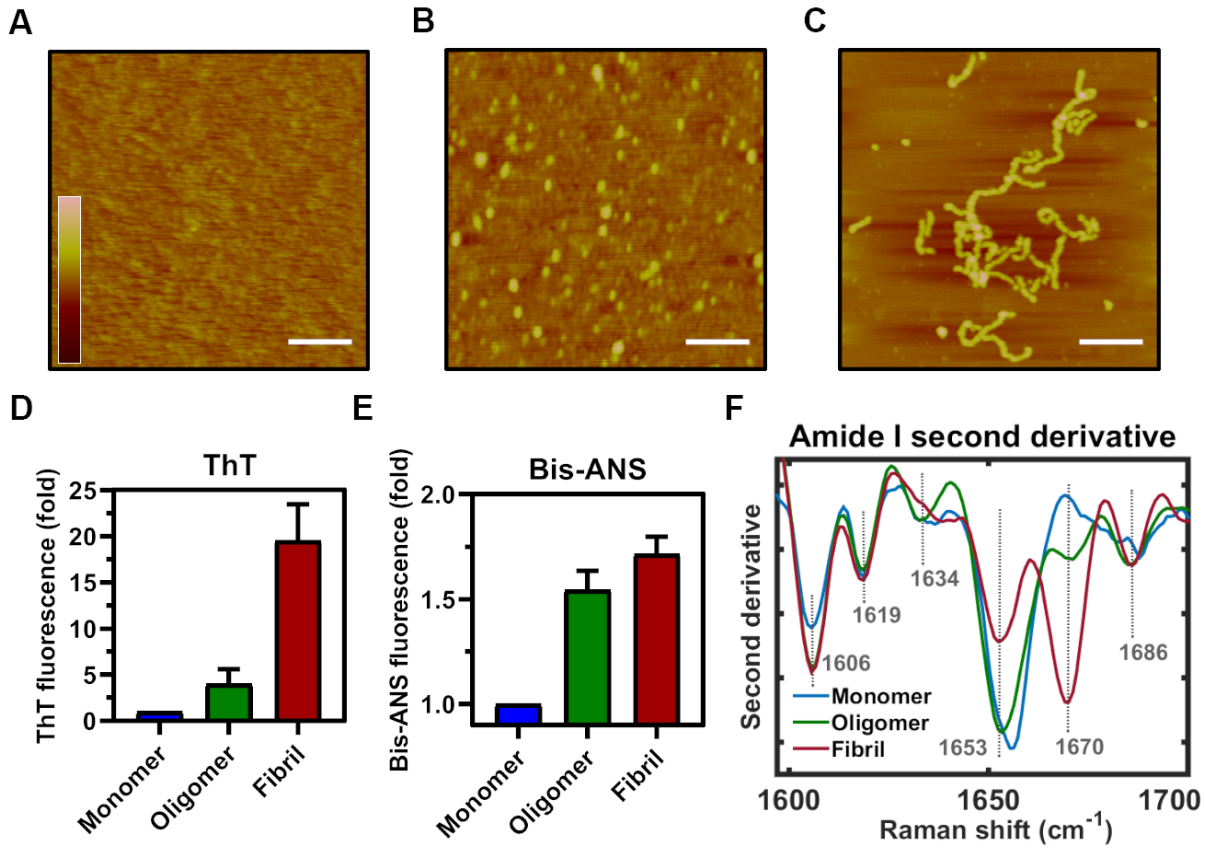

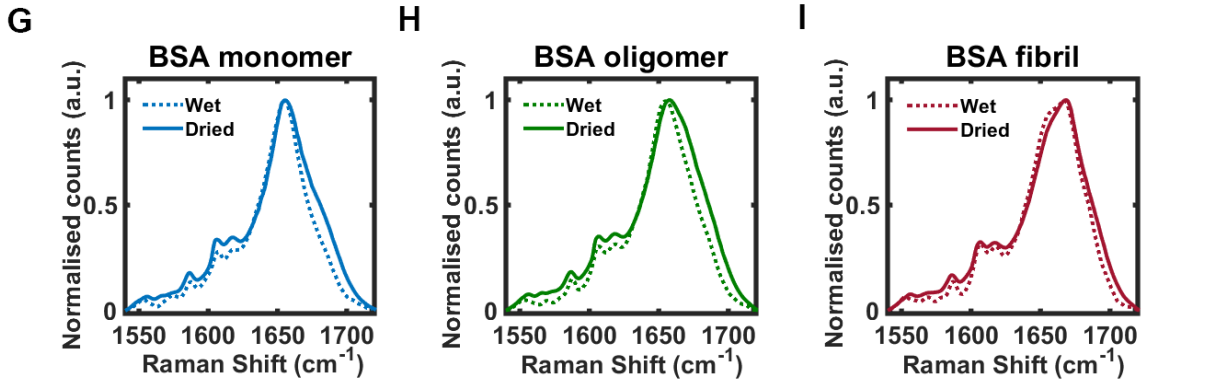

	α-helix		β-sheet		Nonregular	
	Wet	Dried	Wet	Dried	Wet	Dried
Monomer	73	57	0	0	27	24
Oligomer	63	53	31	26	6	21
Fibril	45	44	37	32	18	24

Figure 2 - BSA aggregation species characterisation A-C AFM images of BSA monomer (A), oligomer (B) and fibril (C) samples bound to a mica substrate, z scale bar is 0 – 15 nm, x scale bar = 200 nm. D ThT fluorescence of bulk BSA solution displayed as fold change over monomer fluorescence E Bis-ANS fluorescence of bulk BSA solution displayed as fold change over monomer fluorescence F Amide I second derivative Raman spectra of enriched wet BSA monomer (blue), oligomer (green) and fibril (red) shows changes in frequency of overlapping Amide I peaks as a result of aggregation G-I Amide I spectra shown for enriched BSA monomer (G), oligomer (H) and fibril also compare between wet and dried conditions.

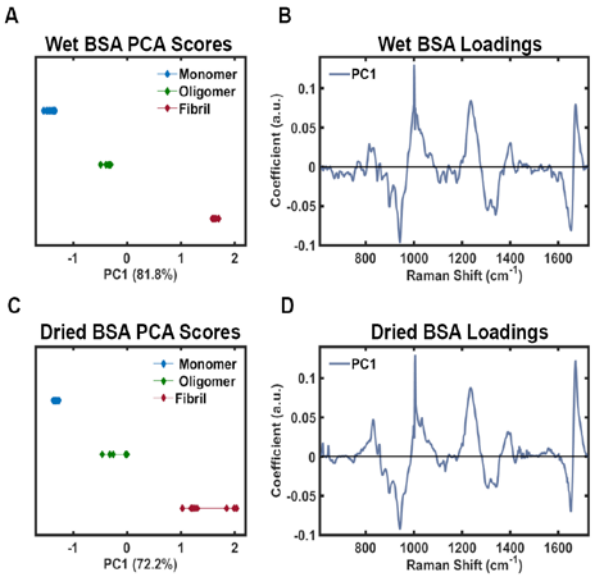

Figure 3 – Principle Component Analysis of BSA Raman spectra A-B PCA of wet BSA Raman spectra A 1-D score scatter plot showing the distribution of monomer spectra (blue diamonds), oligomer spectra (green diamonds) and fibril spectra (red diamonds) across the PC1 axis B PC1 Loadings (blue trace) for PCA of wet BSA Raman spectra highlights spectral variation responsible for scores (loadings x original spectrum = score). C-D PCA of dried BSA Raman spectra C 1-D score scatter plot showing the distribution of monomer spectra (blue diamonds), oligomer spectra (green diamonds) and fibril spectra (red diamonds) across the PC1 axis D PC1 Loadings (blue trace) for PCA of dried BSA Raman spectra highlights spectral variation responsible for scores (loadings x original spectrum = score).

sheet.[52] Here, peaks at 996/1010 cm^{-1} have positive coefficients and therefore increase during aggregation and can be assigned to skeletal β-sheet vibrations. The aromatic amino acids phenylalanine (1001 cm^{-1}) and tyrosine (833 and 860 cm^{-1}) also display positive coefficients for PC1 and therefore increase in intensity during aggregation. Changes in aromatic amino acid environment during aggregation may be due to CH-π interactions or π-π stacking.[53-55] Importantly, the PCA scores plot and loadings for data on dried samples (figures 3C and D respectively) show a very similar pattern as for BSA species in solution and only small frequency shifts are observed in the Amide I, Amide III and skeletal regions, as well as for tyrosine and phenylalanine (listed in supplementary table 2). Together, this suggests that despite the increase in nonregular structure determined by Amide I deconvolution, aggregation species can still be distinguished by the same spectral features irrespective of whether the spectra are measured in wet or dry conditions.

Beta-2 microglobulin (β2M)

β2M is a protein associated with the heavy chains of class I major histocompatibility complex (MHC) that is present on the surface of nucleated cells. The formation of fibrils of β2M is observed in patients with dialysis-related amyloidosis, which is caused by the retention and accumulation of β2M in the plasma during long-term dialysis.[56] β2M was aggregated in citrate buffer at pH 2.5 at a concentration of 1 mg/ml and a temperature of 37°C. The formation of oligomers and fibrils was tracked using AFM (figure 4A-C), ThT (figure 4D) and Bis-ANS (figure 4E) fluorescence. High quantities of spherical oligomers were observed after 24 hours by AFM. Fibrillation proceeded after 2-3 days, and was allowed 14 days to complete. The resulting pellet contained short, needle-like fibrils that were often bundled into higher order structures with heights ranging from 6-20 nm (supplementary figure 1).

Similarly to BSA, a small increase in bulk ThT fluorescence intensity was observed upon β2M oligomer formation, with a strong increase observed after fibril formation (figure 4D). Bis ANS fluorescence intensity was strongly increased upon oligomer formation and remained elevated upon fibril formation (Figure 4E). Respectively, this suggests the formation of cross-β architecture and an increase in hydrophobicity upon aggregation.

The Amide I second derivative spectra shows a common Amide I minima at 1671 cm^{-1} – 1672 cm^{-1}, although this peak increases in intensity (more negative) during aggregation from monomer to oligomer and fibril (Figure 4F), reflected by Amide I band sharpening in the original spectra (Figures 4G-I). Drying by drop deposition appears to have little effect on the β2M Amide I spectra, with the exception of aromatic amino acid intensity in the region of 1530 cm^{-1} – 1620 cm^{-1}. X-ray crystallography has shown that β2M contains an immunoglobulin fold, a domain that consists of two β-sheets made up of 7 antiparallel β-strands.[57-58] The β-sheet content of β2M has been determined at 50% from the crystal structure, and 50% and 55% from vacuum ultra-violet circular dichroism (VUVCD) and IR spectroscopy, respectively.[59] These previous findings are consistent with the Raman spectrum for the β2M monomer (figure 4G), which shows an Amide I peak at 1670/1669 cm^{-1} (wet/dried) and an Amide III peak at 1248/1244 cm^{-1} (wet/dried), as expected for a combination of β-sheet and nonregular secondary structure.[31] The presence of a band in the skeletal region between 980 cm^{-1} and 1020 cm^{-1} provides further indication of a predominantly β-sheet secondary structure, as discussed for BSA aggregation. The β-sheet skeletal band is somewhat masked by the phenylalanine peak ~1004 cm^{-1}, which appears to have a broadened base at ~1010 cm^{-1}. Amide I deconvolution of the wet β2M monomer shows that curve 2, centred at 1671 cm^{-1}, comprises 52% of the Amide I area (table 1). This peak can therefore be assigned to β-sheet structure, in line with previous reports. There is no evidence of α-helical content in the crystal structure of β2M, with ~50% of the secondary structure being assigned to nonregular structures, including turns and loops. Peak 3, centred at 1686 cm^{-1} (15%), can be assigned to nonregular structure, as for BSA. Peak 1, centred at 1654 cm^{-1} (33%) is tentatively assigned to turn structures. Despite overlapping in frequency with α-helical conformation, previous reports using XRC/FTIR[57, 59] do not report any α-helical structure in native β2M. Turns are difficult to assign to proteins by Raman spectroscopy due to their wide range of frequencies throughout the Amide I region.[60] A Raman study of 12 proteins with predefined XRC structures revealed that β-turn vibrations are observed at ~1652 cm^{-1} for Amide I,[61] and the predominantly turn-containing protein Metallothionein has a split Amide I frequency of 1650 cm^{-1} and 1665 cm^{-1}.[62] As for BSA, drying appears to cause a loss in regular secondary structure of the β2M monomer, with peak 2 having an area of 42% (β-sheet), with peak frequencies shifting a maximum of 2 cm^{-1} (table 1). As a result, there is an increase in turn (33% - 35%) and nonregular structure (18% - 23%) in the dried β2M monomer.

Amide I deconvolution of the wet β2M oligomer spectrum shows an overall loss in peak 2 area/β-sheet secondary structure in comparison to the wet β2M monomer (52% – 27%), in favour of increased peak 1/turn structure area (33% – 48%) and peak 3/nonregular structure area (15% – 25%). This aligns with an increase in 940 cm^{-1} intensity in the skeletal region, typically used as a marker for

α-helical structure, although β-turn structured peptides share similar vibrations.[63] Amide I deconvolution of the wet β2M fibril spectrum revealed an increase in peak 2 area/β-sheet secondary structure (27% – 60%) and almost complete loss in peak 3 area/nonregular structure (25% – 3%), which is reinforced by a downshift in Amide III frequency and further broadening of the skeletal peak at

Table 2. Raman Peak assignment

Peak (cm^{-1})	Assignment	Change during aggregation from PCA (relative to CH_2 band)
622	Phenylalanine	-
644	Tyrosine	-
760	Tryptophan	-
830/850	Tyrosine Fermi doublet	↑
880-970	Backbone/Skeletal α-helix	↓
995-1040	Backbone/Skeletal β-sheet	↑
950-992	Backbone/Skeletal nonregular/turns	-
1002	Phenylalanine	↑ ↔
1033	Phenylalanine	-
1068	Tryptophan	-
1080	CC/CN/CO/phenylalanine	-
1104	CC/CN/CO	↓
1128	CC/CN	-
1158	CC	-
1177	Tyrosine/Phenylalanine	-
1208	Tyrosine	↑
1220-1240	Amide III β-sheet	↑
1280-1320	Amide III α-helix	↓
1250-1270	Amide III nonregular/turns	-
1320	$C_\alpha H$	-
1342	$C_\alpha H$/Tryptophan	-
1362	Tryptophan	-
1404	CO_2-	-
1425	CH	-
1450	CH	-
1466	Tryptophan	-
1551	Tryptophan	-
1581	Phenylalanine/Tryptophan	-
1605	Phenylalanine	-
1618	Tyrosine/Tryptophan/ Phenylalanine	-
1653-1656	Amide I α-helix	↓
1653-1667	Amide I nonregular/turns	-
1669-1674	Amide I β-sheet	↑
1675-1694	Amide I nonregular/turns	-

Key: ↑ peak increases in intensity, ↓ peak decreases in intensity, ↔ peak broadens, - no consistent change

1010 cm^{-1} in comparison to the monomer and oligomer spectra (supplementary figure 2). Despite a loss in β–sheet structure in monomeric β2M upon drying, peak 2 area/β-sheet structure is increased in the dried β2M oligomer in comparison to the wet β2M

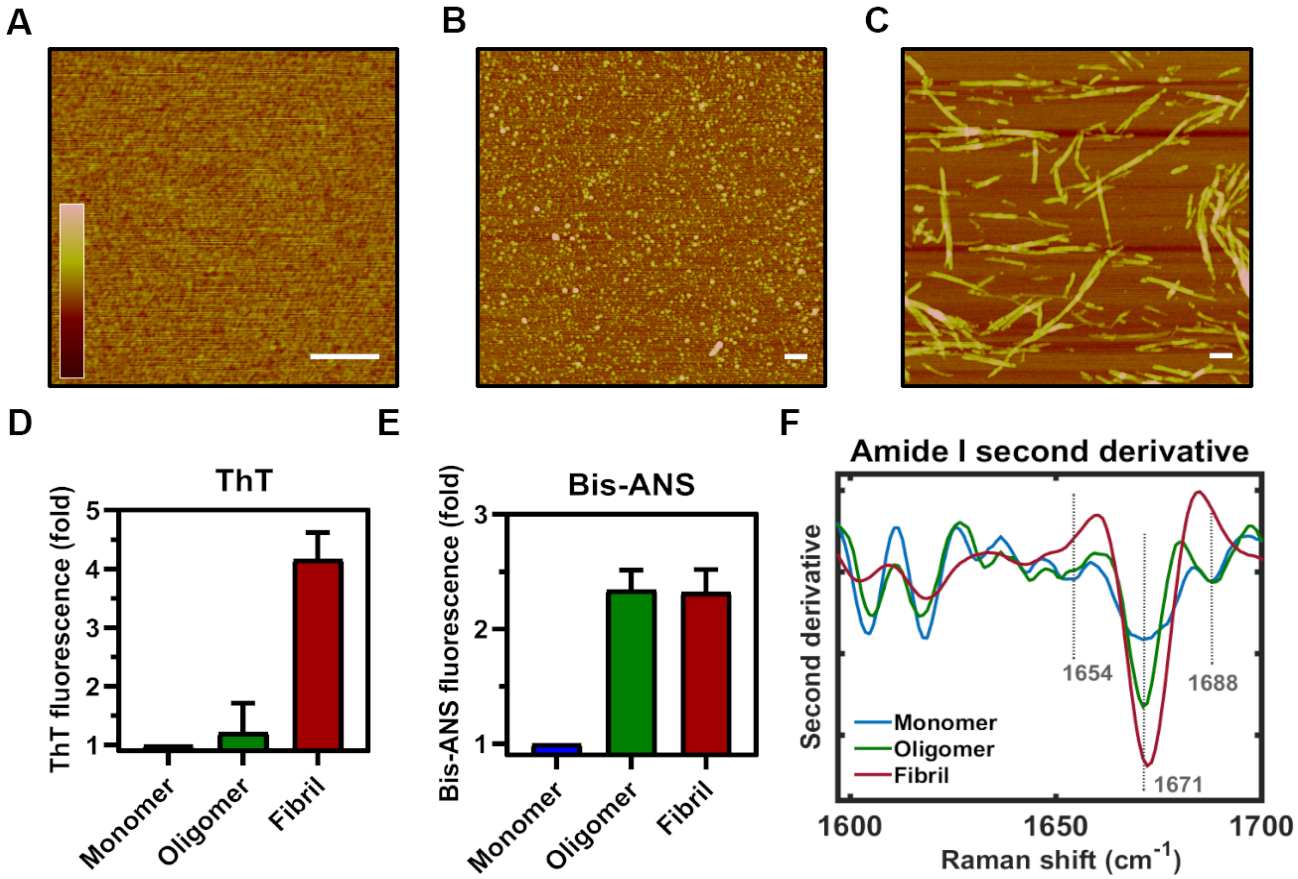

	Turn		β-sheet		Nonregular	
	Wet	Dried	Wet	Dried	Wet	Dried
Monomer	33	35	52	42	15	23
Oligomer	48	48	27	33	25	19
Fibril	37	33	60	66	3	1

Figure 4 – β2M aggregation species characterisation A-C AFM images of β2M monomer (A), oligomer (B) and fibril (C) samples bound to a mica substrate, z scale bar is 0 – 8 nm (monomer), 0 – 15 nm (oligomer) and 0 – 35 nm (fibril), x scale bar = 200 nm. D ThT fluorescence of bulk β2M solution displayed as fold change over monomer fluorescence. E Bis-ANS fluorescence of bulk β2M solution displayed as fold change over monomer fluorescence. F Amide I second derivative Raman spectra of enriched wet β2M monomer (blue), oligomer (green) and fibril (red) shows changes in frequency of overlapping Amide I peaks as a result of aggregation. G-I Amide I spectra are shown for enriched β2M monomer (G), oligomer (H) and fibril (I) and compare between wet and dried conditions.

structure (27% - 33%), as well as for the fibril (60% - 66%), suggesting that the drying process accelerates aggregation for oligomeric and fibrillar β2M.

One principle component (PC1) is required to sufficiently separate the Raman spectra of each of the wet β2M aggregation species by PCA (figure 5A). Monomeric spectra have a highly negative score for PC1 (< -4), oligomeric spectra have a slightly negative score (-2 – -4), and fibrillar spectra have a positive score. The loadings for PC1 (figure 5B) reveals that peaks indicating β-sheet secondary structure have a strong positive coefficient including 1673 cm^{-1} (Amide I), 1227 cm^{-1} (Amide III), 1008 cm^{-1} and 998 cm^{-1} (skeletal). Peaks in the loadings spectra with a negative coefficient for PC1 represent nonregular structures which include frequencies at 1645 cm^{-1} (Amide I), 1287 cm^{-1} (Amide III), and 943 cm^{-1} (skeletal). This is expected as the scores plot shows an increase in PC1 score as β2M aggregates wherein β-sheet structures increase likely at the expense of non-regular and other structures. Similarly to BSA, tyrosine and phenylalanine intensities also increase in relation to the CH2 band during β2M aggregation (828 cm^{-1}, 856 cm^{-1} and 1002 cm^{-1} respectively).

Two principle components are required to sufficiently separate dried β2M spectra (Figure 5C). PC1 is similar as for the spectra of wet β2M species, but inverted, so that monomeric β2M spectra have a positive score for PC1 and fibrillar spectra have a negative score. PC1 frequencies remain similar, with β-sheet features; 1673 cm^{-1} (Amide I), 1227 cm^{-1} (Amide III), 1008 cm^{-1} and 998 cm^{-1} (skeletal), being identical. PC2 is necessary to distinguish β2M oligomeric spectra (negative score) and fibrillar spectra (positive score). The increase in β-sheet structure observed in β2M oligomers and fibrils upon drying may be responsible for the oligomers becoming more fibril-like in the PC1 axis. PC2 Peaks with a positive coefficient in the Amide I (1672 cm^{-1} and 1675 cm^{-1}) and Amide III region (1225 cm^{-1}, 1228 cm^{-1}) explain monomeric/fibrillar β2M and β-sheet structure. The peaks with negative coefficients include a larger range of both β-sheet and nonregular/turn structures, suggesting that β2M oligomers are more structurally heterogeneous than β2M monomers and fibrils; e.g. Amide III peaks (1238 cm^{-1},1244 cm^{-1}, 1267 cm^{-1}, 1290 cm^{-1}). As for BSA, the PCA results show that despite a change in conformation determined by Amide I deconvolution, aggregation species can still be classified using the same spectral features in wet and dried β2M spectra.

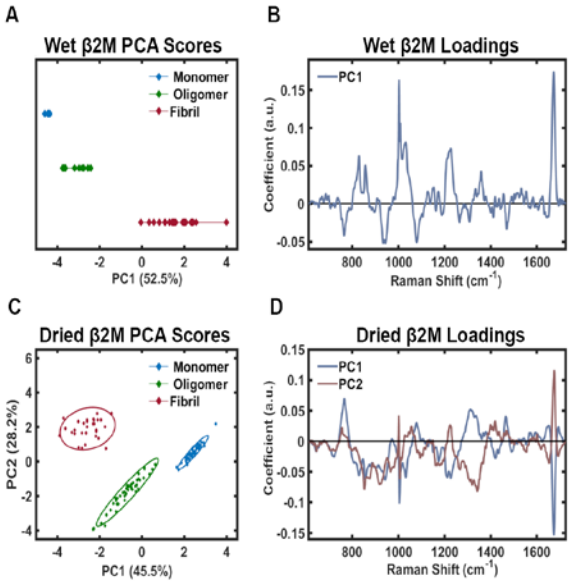

Figure 5 – Principle Component Analysis of β2M Raman spectra A-B PCA of wet β2M Raman spectra A 1-D score scatter plot showing the distribution of monomer spectra (blue diamonds), oligomer spectra (green diamonds) and fibril spectra (red diamonds) across the PC1 axis B PC1 Loadings (blue trace) for PCA of wet β2M Raman spectra highlights spectral variation responsible for scores (loadings x original spectrum = score). C-D PCA of dried β2M Raman spectra C 2-D score scatter plot showing the distribution of monomer spectra (blue diamonds), oligomer spectra (green diamonds) and fibril spectra (red diamonds) across the PC1 and PC2 axes D PC1 Loadings (blue trace) and PC2 loadings (red trace) for PCA of dried β2M Raman spectra highlights spectral variation responsible for scores (loadings x original spectrum = score).

Tau

Tau is a microtubule-associated protein (MAP) that is primarily found in neuronal axons where it plays a role in the stabilization of microtubules.[64] The pathological aggregation of tau into soluble and insoluble oligomers and insoluble filaments is observed in a range of neurodegenerative diseases that are collectively termed tauopathies. Each disease can be characterised by specific patient symptoms and distinctive patterns of pathology.[65] Furthermore, there is increasing evidence from electron cryo-microscopy to suggest that the conformation of tau filaments may be unique to each Tauopathy.[66-67] In this study we wanted to use Raman spectroscopy to study the conformational changes that occur as monomeric tau aggregates first into oligomers and finally into filaments, as it is believed to do *in vivo* in tauopathies. Monomeric tau is an intrinsically disordered protein, meaning that it is made up predominantly of nonregular structure as opposed to stable secondary structural elements including α-helices and β-sheets. Disordered proteins are typically rich in charged and polar amino acids, leading to characteristically low hydrophobicity and therefore a high level of solubility. Electrostatic repulsion prevents the spontaneous self-association of full-length tau *in vitro* and this may also play a role in preventing tau aggregation *in vivo* in physiological conditions. The factors that overcome this repulsion to aggregate *in vivo* are unclear but negatively charged molecules including heparin[68] have been used to aggregate tau *in vitro*. This suggests that electrostatic interactions are important to the initiation of polymerization and charge neutralization may be a key driver of tau aggregation. Here, heparin was used as a cofactor to induce tau fibrillation at a Molar ratio of 1:2 (heparin:protein). Tau oligomers were formed after 4 hours of incubation, whereas tau filaments were allowed 8 days to form. AFM images of each of the aggregation species are shown in figure 6A-C and heparin alone is shown in supplementary figure 4. Tau oligomers are spherical in morphology with an average height of ~2-4 nm, whilst tau fibrils are long and curved with an average height of ~7-8 nm (supplementary figure 1).

No change in bulk ThT fluorescence intensity was observed upon β2M oligomer formation, but a strong increase observed after fibril formation (figure 6D), suggesting that the tau oligomers do not form detectable regular cross-β architecture. Bis ANS fluorescence intensity was strongly increased upon oligomer formation and remained elevated upon fibril formation (Figure 6E), as observed for BSA and β2M, confirming an increase in tau hydrophobicity upon oligomerisation. This common pattern of ThT/Bis-ANS binding can be employed as a useful tool to track protein aggregation and identify the aggregation species that are present whereby monomer = ThT: low, Bis-ANS: low, oligomer = ThT: low, Bis-ANS: high

and fibril = ThT: high, Bis-ANS: high (relative levels). This response has been observed previously for tau using Thioflavin S and ANS fluorescence.[69]

The second derivative Raman spectra show that the tau monomer has two minima at 1683 cm-1 and 1674 cm^{-1} that shift to 1685 cm-1 and 1670 cm^{-1} in the tau oligomer, indicating the formation of β-

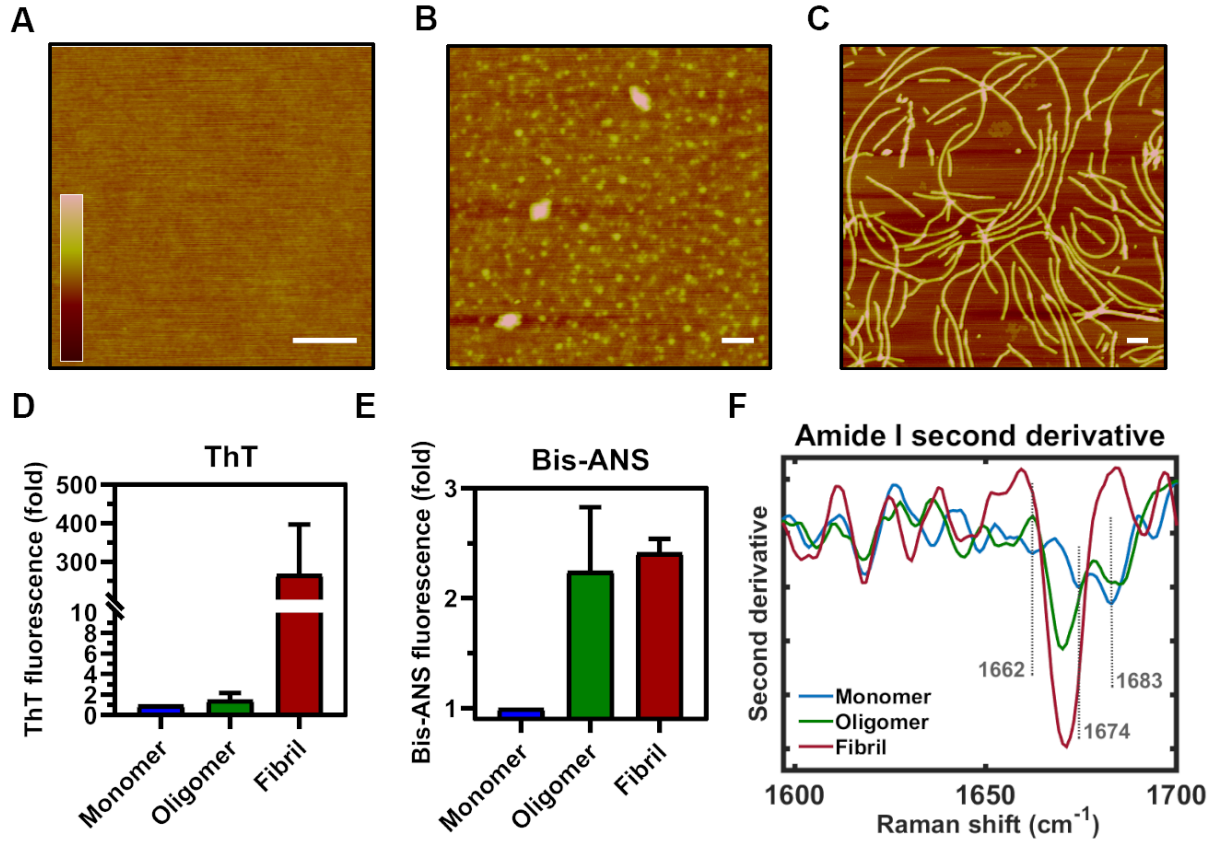

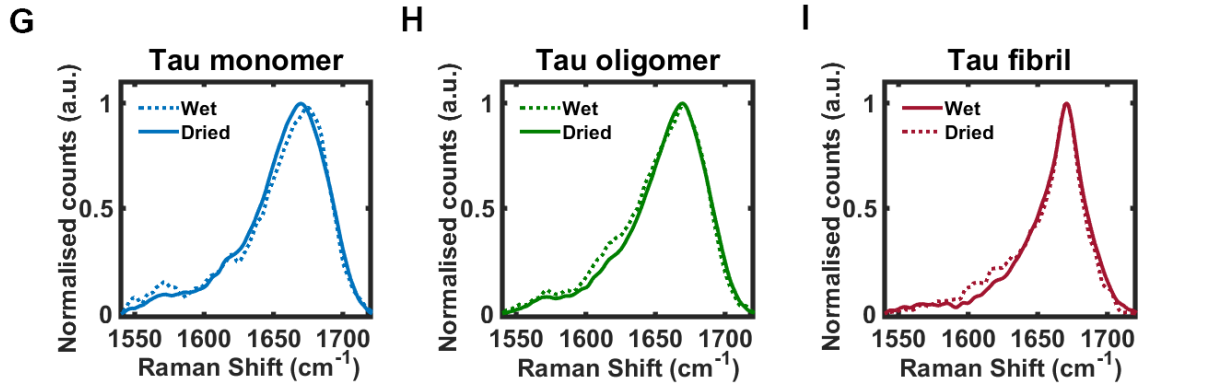

	α-helix/turn		β-sheet		Nonregular	
	Wet	Dried	Wet	Dried	Wet	Dried
Monomer	0	38	0	31	100	31
Oligomer	38	41	23	36	39	23
Fibril	41	35	49	42	10	23

Figure 6 – Tau aggregation species characterisation A-C AFM images of Tau monomer (**A**), oligomer (**B**) and fibril (**C**) samples bound to a mica substrate, z scale bar is 0 – 15 nm, x scale bar = 200 nm. **D** ThT fluorescence of bulk Tau solution displayed as fold change over monomer fluorescence **E** Bis-ANS fluorescence of bulk Tau solution displayed as fold change over monomer fluorescence **F** Amide I second derivative Raman spectra of enriched wet Tau monomer (blue), oligomer (green) and fibril (red) shows changes in frequency of overlapping Amide I peaks as a result of aggregation. **G-I** Amide I spectra are shown for enriched Tau monomer (**G**), oligomer (**H**) and fibril (**I**) and compare between wet and dried conditions.

sheet secondary structure. The tau fibril spectrum is dominated by a large component at 1671 cm^{-1}, with a very small shoulder at 1681 cm^{-1}. As tau doesn't have a regular structure, it is not amenable to

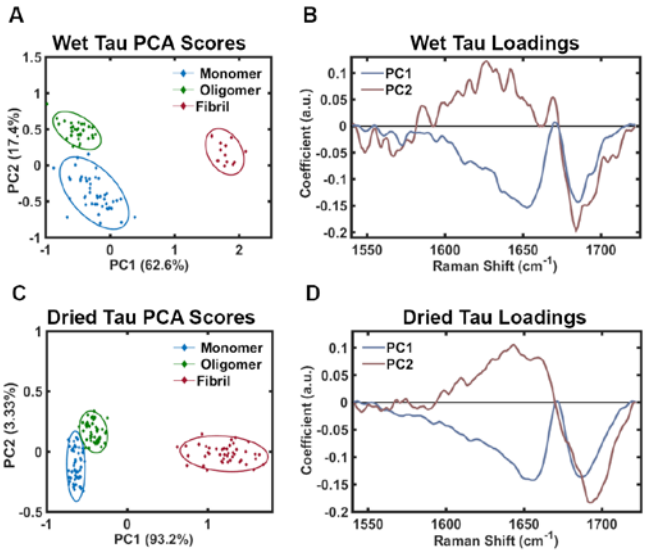

Figure 7 – Principle Component Analysis of Tau Raman spectra A-B PCA of wet Tau Raman spectra A 2-D score scatter plot showing the distribution of monomer spectra (blue diamonds), oligomer spectra (green diamonds) and fibril spectra (red diamonds) across the PC1 and PC2 axes B PC1 Loadings (blue trace) and PC2 loadings (red trace) for PCA of wet Tau Raman spectra highlights spectral variation responsible for scores (loadings x original spectrum = score). C-D PCA of dried Tau Raman spectra C 2-D score scatter plot showing the distribution of monomer spectra (blue diamonds), oligomer spectra (green diamonds) and fibril spectra (red diamonds) across the PC1 and PC2 axes D PC1 Loadings (blue trace) and PC2 loadings (red trace) for PCA of dried Tau Raman spectra highlights spectral variation responsible for scores (loadings x original spectrum = score).

crystallization and hence, an accurate crystal structure reference for secondary structure composition is unavailable. Therefore, we applied the same Amide I curve fit parameters to tau that were applied to both BSA and β2M. Unlike BSA and β2M, the tau monomer Amide I spectrum shows a considerable shift in frequency from 1675 cm^{-1} to 1669 cm^{-1} upon drying (Figure 6G). It has been shown that film deposition causes greater structural changes in disordered proteins than globular proteins, which is likely due to disordered proteins having less native intramolecular hydrogen bonding in favour of intermolecular hydrogen bonds with water molecules.[70] Deconvolution of the Amide I region of the wet tau monomer spectrum reveals that each peak has a frequency correlating to nonregular structure; 1663 cm^{-1} (59%)[61, 71], 1674 cm^{-1} (2%), 1683 cm^{-1} (39%). Drop-deposition leads to a shift in these peaks to the following frequencies: 1655 cm^{-1} (38%), 1671 cm^{-1} (31%) and 1687 cm^{-1} (31%). A similar change in peak 2 frequency was observed upon BSA drop-deposition, which showed a downshift from 1675 cm^{-1} to 1667 cm^{-1}. The 1667 cm^{-1} peak in dried BSA was assigned to non-hydrated nonregular structure. However, the frequency at 1671 cm^{-1} aligns with β-sheet structure seen in β2M species and aggregated BSA. This suggests that drop deposition leads to the formation of regular secondary structure in monomeric tau and/or aggregation. The peak in the wet tau spectrum at 1663 cm^{-1} is assigned to nonregular structure, whilst the peak in the dried tau spectrum at 1655 cm^{-1} may account for α-helical or turn structure. Oligomerisation leads to a downshift of this peak from 1663 cm^{-1} – 1657 cm^{-1} for wet tau , suggesting that the tau oligomer adopts regular α-helical or turn structure. Oligomerisation also leads to a shift in peak 2 frequency from 1674 cm^{-1} to 1670 cm^{-1} in the wet tau spectrum (23% area) and finally, this peak shifts to 1671 cm^{-1} in the wet fibril spectrum (49% area). Similarly, the dried spectra show and increase in peak 2/β-sheet structure upon oligomerisation (31% – 36%), and fibril formation (36% – 42%). Together, this shows that tau adopts β-sheet structure upon aggregation, as seen previously for tau oligomers[6] and for filaments.[72-74] Tentative analysis of the Amide III and skeletal regions reinforces these results (supplementary figure 3). Despite spectral contamination from heparin, a downshift in Amide III and an upshift in skeletal vibrations are observed during aggregation, both of which signify an increase in β-sheet structure, as described for BSA and β2M.

For principal component analysis only the Amide I region of the Raman spectra was used since heparin, used for aggregation of Tau, contains a number of Raman peaks throughout the fingerprint region, but is featureless in the Amide I region (supplementary figure 6). 2 PCs were required to separate the data classes for wet tau spectra (figure 7A). The PC1 axis separates monomeric and oligomeric spectra, which have primarily negative scores, from the positively scored fibrillar spectra. PC2 is also required to separate monomeric spectra (negative score) from oligomeric spectra (positive score). The loadings for the PCA are shown in figure 7B. PC1 shows negative peaks at 1653 cm^{-1} and 1686 cm^{-1} corresponding to turn/α-helical and nonregular structure respectively, aligning with monomeric and oligomeric spectra. PC1 has a positive peak at 1670 cm^{-1}, corresponding to β-sheet structure and aligning with fibrillar spectra. Tau monomers and oligomers can be separated across the PC2 axis. Monomers have a negative PC2 score and oligomers have a positive PC2 score. The loadings for PC2 show a negative peak at 1686 cm^{-1} assigned to nonregular structure and a positive peak at 1669 cm^{-1} corresponding to β-sheet structure, reinforcing the results from Amide I deconvolution.

The PCA scores and loadings for dried tau samples (Figure 7C and D) are similar to those for tau species in solution. The monomer and oligomer spectra show less separation across the PC2 axis, likely due to the loss of the positive 1669 cm^{-1} component observed in the PC2 loadings for wet tau. This is because drying the tau monomer leads to a downshift in Amide I frequency so that it matches the frequency of that of the dried tau oligomer, as discussed previously. Although Amide I deconvolution showed a large change in monomeric tau secondary structure upon drop-deposition, dried tau monomers, oligomers and fibrils can still be classified by PCA.

Cross analysis of oligomeric and fibrillar protein species

We so far have demonstrated that Raman spectroscopy can be used to characterise distinct aggregation species from the α-helical-rich protein BSA, the β-sheet rich protein β2M and the natively disordered protein tau. Next we looked to directly compare monomeric, oligomeric and then fibrillar species of each protein to ascertain whether they too can be distinguished from each other using their Raman spectral signatures. As each protein has a different primary sequence and hence, amino acid content, we excluded the entire spectrum outside of the Amide I band, so that any differences that are observed can be assigned directly to secondary structure (1630 - 1720 cm^{-1}). In order to determine whether the spectral components that distinguish the proteins are conserved upon drying, we have included both wet and dried protein spectra in our analysis. PCA was applied to the Amide I spectra of the monomeric proteins, leading to separation BSA, β2M and tau spectra (Figure 8A). BSA

monomers have a positive score for PC1 (> 1), whilst tau monomers have a negative score and β2M monomers have on average a slightly positive score (< 1). The loadings for PC1 show a positive peak at 1653 cm^{-1} and a negative peak at 1682 cm^{-1}, assigned to α-helical structure and non-regular structure respectively (figure 8B). Therefore, spectra for proteins rich in α-helical structure have a positive score (e.g. BSA) and spectra for proteins with a nonregular structure have a negative score (e.g. tau), whilst spectra for proteins with equal quantities of each of these components have a score close to zero (e.g. β2M). As determined by Amide I deconvolution, dried BSA monomers have increased nonregular structure (wet = 3%, dried = 24%), which is reflected by the decrease in PC1 score for dried spectra in the scores plot, also representing an increase in nonregular structure. PC3 enables the complete separation of wet tau (green diamonds, negative score) and β2M monomers (positive score), explained by the positive peak at 1668 cm^{-1} and the negative peak at 1684 cm^{-1} in the loadings. This component also leads to the separation of wet (negative PC3) and dried (positive PC3) tau monomers, as dried tau monomers have an Amide I frequency of 1669 cm^{-1}, as opposed to 1675 cm^{-1} for tau in solution (Figure 6G). Wet and dried β2M spectra are not separated by PC1 and PC3; this is expected as there was very little change in the β2M Amide I spectrum upon drying (Figure 4G). This demonstrates that each monomeric protein can be distinguished by its Amide I region alone, whether the protein is wet or dried.

Next, PCA was applied to oligomeric protein spectra to understand the subtle underlying features that cause the variation (figure 8C). Two principle components were required to separate the oligomeric Amide I spectra of each protein. Oligomeric β2M spectra can be separated from oligomeric BSA and tau spectra across the PC1 axis, with the PC2 axis also being required to separate oligomeric BSA and tau spectra. The PC1 axis separates β-sheet components (1672 cm^{-1} negative coefficient), from α-helical and nonregular components (1650 cm^{-1} and 1686 cm^{-1} positive coefficient). Therefore, β2M oligomer spectra have negative PC1 scores, whilst BSA and tau oligomers have a positive PC1 score. Oligomeric BSA spectra have a positive PC2 score, corresponding to a peak at 1652 cm^{-1} (α-helix) in the loadings plot (Figure 8D), whereas oligomeric tau spectra have a slightly negative PC2 score, corresponding to a peak at 1678 cm^{-1} (nonregular) in the loadings plot. β2M spectra have a mixed slightly positive and slightly negative score for PC2. This is consistent with the results from Amide I deconvolution, as tau oligomers are rich in nonregular structure (wet = 39%, dried = 23%) in comparison to BSA oligomers (wet = 6%, dried = 21%),

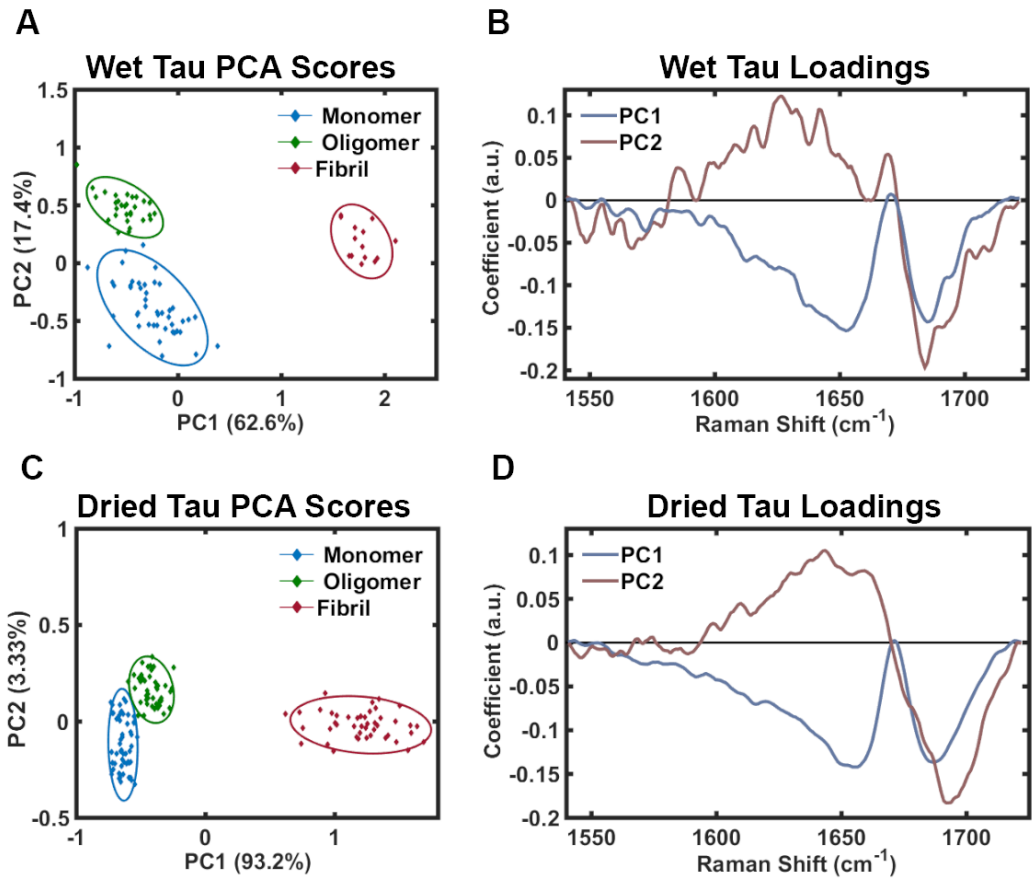

Figure 8 – Principle Component Analysis of Tau Raman spectra A-B PCA of wet Tau Raman spectra A 2-D score scatter plot showing the distribution of monomer spectra (blue diamonds), oligomer spectra (green diamonds) and fibril spectra (red diamonds) across the PC1 and PC2 axes B PC1 Loadings (blue trace) and PC2 loadings (red trace) for PCA of wet Tau Raman spectra highlights spectral variation responsible for scores (loadings x original spectrum = score). C-D PCA of dried Tau Raman spectra C 2-D score scatter plot showing the distribution of monomer spectra (blue diamonds), oligomer spectra (green diamonds) and fibril spectra (red diamonds) across the PC1 and PC2 axes D PC1 Loadings (blue trace) and PC2 loadings (red trace) for PCA of dried Tau Raman spectra highlights spectral variation responsible for scores (loadings x original spectrum = score).

with β2M oligomers containing moderate amounts of nonregular structure (wet = 25%, dried = 19%). This demonstrates that like monomers, the oligomers of each protein can be successfully distinguished based entirely on their conformational signature for proteins both wet and dried.

Next we compared the fibrillar species of each protein to determine whether like the oligomers of each protein, the fibrils can similarly be distinguished using their spectral signatures. Again, only the Amide I band was used for analysis, so that any differences that are observed can be assigned directly to secondary structure. PCA was applied to the Amide I spectra of the fibrillar protein species (Figure 8E). Two principle components were required to separate the Amide I spectra for each protein fibril. Fibrillar BSA spectra can be separated from fibrillar β2M and tau spectra across the PC1 axis, with the PC2 axis required to completely separate fibrillar β2M and tau spectra. Fibrillar β2M spectra have a positive PC1 score, with the loadings showing positive coefficients at 1675 cm^{-1}, in this case assigned to β-sheet secondary structure (Figure 8F). Fibrillar BSA spectra have a negative PC1 score and fibrillar tau spectra a slightly negative PC1 score, with the loadings showing a negative coefficient at 1654 cm^{-1} and 1687 cm^{-1}, assigned to α-helical and nonregular structure respectively. This aligns well with the results from Amide I deconvolution, which showed a high β-sheet content in β2M fibrils (wet = 60%, dried = 66%) followed by tau fibrils (wet 49%, dried 42%), with BSA fibrils having the lowest β-sheet content (wet = 37%, dried = 32%). Fibrillar BSA and β2M spectra have a negative PC2 score, whereas fibrillar tau spectra have a positive PC2 score. The PC2 loadings show that components at 1668 cm^{-1} 1690 cm^{-1} both have positive coefficients, whereas negative components include 1655 cm^{-1} and 1676 cm^{-1}. This aligns with the results from Amide I deconvolution, as the β2M fibril spectrum have a higher frequency β-sheet peak (wet = 1673 cm^{-1}, dried = 1674 cm^{-1}) than tau fibrils (1671 cm^{-1}), whilst the 1655 cm^{-1} component explains the negative score for the BSA fibril spectra. This shows that like monomers and oligomers, the fibrils of the three different proteins had sufficiently different Raman spectral signatures that could serve as their unique conformational fingerprint, further highlighting that the drying process does not prevent the structurally diagnostic advantage of Raman spectroscopy for the identification and characterisation of amyloidogenic protein species.

DISCUSSION

We have demonstrated that Raman spectroscopy is an effective tool for the direct conformational analysis of proteins and can provide a unique label-free conformational fingerprint for distinct protein conformers, whether they are monomers, oligomers or fibrils. Since conformation is believed to underpin the toxic potential of many misfolded proteins, such a conformational signature can serve as a vital probe for detecting, as well as targeting, toxic protein conformers in proteinopathies such as Alzheimer's disease.

Here, we have deconvolved the Amide I band of the Raman spectrum in order to quantitatively determine the secondary structural content of α-helical-rich BSA, β-sheet-rich β2M and natively disordered tau during their aggregation from monomers, into oligomers and finally fibrils. This was achieved by developing a fitting routine that closely replicated the secondary structural content of BSA and β2M obtained from X-ray crystallography. The same fitting routine was then applied to the Amide I band of oligomeric and fibrillar species in order to track secondary structural evolution. The fitting routine was then applied to tau, which is not amenable to crystallography due to lack of structural order.[75-76] In all cases, spectral evolution highlighting conformational change was observed throughout aggregation resulting in an increase in β-sheet secondary structure in fibrillar species, regardless of the native monomeric conformation. Nevertheless, apart from the increase in β-sheet structure observed during protein aggregation, Amide I deconvolution also shows that the oligomeric and fibrillar species of each protein actually maintains a high degree of the native monomeric secondary structure. For example, BSA oligomers and fibrils maintain a high degree of α-helical structure, as do higher-order tau species with nonregular structure and β2M with β-sheet. This underlines that amyloidogenic aggregation does not require the complete restructuring of a protein, with partial folding/unfolding being sufficient to drive aggregation.[77-82]

In order to assess the utility of drop-deposition Raman spectroscopy (DDRS) for protein species characterisation, we analysed samples both in the wet and dried state for comparison. DDRS is of interest for biomedical applications as it is an effective means of background removal from Raman spectra enabling rapid data acquisition and processing whilst using minimal sample (0.5 μl in this study). It is unlikely that Raman spectroscopy of wet protein samples would be amenable for use in medical diagnostics, whereas DDRS is far more suitable.[83-84] Here, we have demonstrated that despite small changes in conformation upon drying, proteins retain a conformational fingerprint that enables them to be distinguished from other proteins and other protein species (e.g. monomer, oligomer, fibril). The conformational change caused by drying is much larger for nonregular/intrinsically disordered proteins, such as tau, in comparison to globular proteins, such as BSA and β2M. Despite this, dried tau monomers, oligomers and fibrils can still be classified based on their conformational fingerprint using both deconvolution and PCA.

An earlier characterisation of morphologically distinct β2M fibrils by FTIR revealed a decrease in β-sheet content upon aggregation of the monomeric protein (55% β-sheet) into the 'long straight' fibril (51% β-sheet) or 'worm-like' fibril (53%).[59] This contrasts with the results from our study, in which we find that the β-sheet content of β2M monomers increases from 52% to 60% upon fibril formation. However, the β2M fibrils formed by Hiramatsu *et al* were formed by a seeding reaction, in which preformed fibrils 'template' their conformation onto native monomers, greatly increasing the kinetics of fibrillation. However, selection pressures during the seeding process have been shown to lead to the emergence of specific populations of fibril conformation,[85-86] which may explain the observed differences in structure.

In general, Raman spectroscopy has been scarcely applied to study conformations in Tau. In one of the few previous studies UV *resonance* Raman spectroscopy (UVRRS) was applied to understand fibril formation in a fragment of tau that consists of the four repeat-domain regions of the protein that constitute the fibril core (tau4RD).[87] Fragments can behave differently than the native (full length) protein. Nevertheless, since UV coincides with the electronic transition of proteins (resonance), resonance enhancement of certain features in the Raman spectrum occurs, enabling lower concentrations of proteins to be probed in comparison to spontaneous Raman spectroscopy. However, this enhancement can vary between bands meaning a resonant spectrum often differs from that seen in spontaneous Raman and UV-radiation can cause sample damage very easily which can confound results. Ramachandran *et al* observed changes in band frequency that were assigned to an increase in β-sheet over time, but the relatively weak enhancement of the Amide I band prevented its deconvolution and therefore conformational assignment. Here, we have shown that filaments of full-length, wild-type tau (2N4R) contain β-sheet secondary structure (49%), but retain a large amount of non-regular structure. Sim-

ilar results have been observed previously using FTIR, with tau fibrils shown to contain ~40% β-sheet secondary structure and mutant tau fibrils (P301L/V337M) shown to contain significantly more β-sheet.[74] Furthermore, tau filaments that were purified from the brain of a deceased patient with Down's syndrome showed ~57% β-sheet from FTIR.[72] Together, this demonstrates the dependence of fibrillar conformation on aggregation conditions.

It is now understood that the misfolded structure of amyloidogenic proteins varies between different diseases, even if the aggregate is formed from the same protein.[88] These different conformations formed from the same protein are termed 'strains'[89-97] or 'conformers'.[98-101] The concept of conformationally distinct "strains" arose in the prion field, but it is now believed to be a feature shared by many misfolded proteins and is not restricted to the prion protein. Thus far the evidence to support the hypothesis that tau can acquire different conformations as it forms different "strains" or "conformers" has come from morphological studies showing distinct morphologies of tau aggregates,[88, 91] immunological studies demonstrating that different tau aggregates display distinct conformation-sensitive epitopes[102-104] and, most recently from cryo-EM studies showing ultra-structural differences between tau filaments.[66-67] Here we explore whether Raman spectroscopy, a relatively much simpler technique compared to cryo-EM, may be a useful technique to quantitatively characterise protein strains, as shown previously for morphologically distinct strains of PrP,[105] β2M,[59] and α-synuclein mutants.[29] Since the data obtained from Raman spectroscopy provides direct insight into the conformational composition of distinct aggregates with almost no sample preparation, it can greatly augment studies for the differential detection of different protein conformers. Furthermore since it is a label-free approach, it will provide structural information without confounding influences of protein-tags, which are often an integral part of other aggregation assays.

The Raman spectrum of a protein is rich in information and provides more than secondary structural content. The combination of Raman spectroscopy and PCA enables the classification of spectral regions that are associated with a particular protein or aggregation species. We have shown that a maximum of two principle components are required to sufficiently classify morphologically distinct aggregation species of BSA, β2M and tau. Furthermore, oligomeric, as well as fibrillar, species of each protein could be classified based on the Amide I region alone. For proteins with identical primary sequences, the whole fingerprint region of the Raman spectrum could be used for structural analysis (including tertiary structural markers) and more principle components can be applied to correctly classify the data if required. Therefore, PCA can be a particularly powerful technique for distinguishing and characterizing protein conformers with subtle differences in secondary or tertiary structure. This is highlighted by recent applications of Raman spectroscopy and PCA in disease diagnostics.[106-110] Nevertheless, the initial characterisation of pure samples is essential for the development of chemical fingerprints that can be applied to such classification models in complex systems in order to develop an understanding of any differences that are observed.

CONCLUSION AND PERSPECTIVES

Aggregation of proteins into distinct conformations is believed to underpin the pathogenic properties of many misfolded proteins in proteinopathies – from seeding competence and propagation of disease, to inherent toxic potential of toxic species. Various lines of evidence support this hypothesis and provide direct and indirect evidence for the distinct conformations acquired by protein aggregates in disease. The recent high resolution electron cryo-microscopy (cryo-EM) maps of tau filaments from Alzheimer's disease[66] and Pick's disease[67] reveal distinct folds in the filaments from each disease, unambiguously substantiating the presence of molecular conformers in tauopathies. Though providing invaluable insight into the ultrastructure of aggregates, cryo-EM is an inherently slow and laborious process, meaning high-throughput and large scale analysis of the numerous tau conformers implicated in tauopathies, or indeed other protein strains implicated in other proteinopathies, is not practically feasible with this technique. Raman spectroscopy offers a rapid, high-throughput means of characterising and classifying molecular conformers both *in vitro*, *ex vivo* and potentially *in vivo*. Here we provide the first evidence of the utility of drop-deposition Raman spectroscopy for the differential detection of both oligomers and fibrils of three different amyloidogenic proteins, including tau, whose aggregates have never before been interrogated using spontaneous Raman spectroscopy. Although on drying by drop-deposition has some effect on the conformational fingerprint compared to corresponding wet samples, substantial conformational information is retained and more significantly allows distinction between aggregation species within and between different proteins. We postulate that Raman spectral signatures of distinct conformers (oligomers or fibrils) of amyloidogenic proteins can serve as a unique and label-free fingerprint for their differential detection. In the case of tauopathies this will be vital for early diagnosis, better understanding of the role of conformation in conferring pathogenic potential of different tau conformers, and ultimately for the design of conformer-specific disease-modifying therapies.

MATERIALS AND METHODS

Tau purification

All buffer reagents are from Sigma unless otherwise stated. pET-29b tau plasmid (addgene, NM_005910) was transfected into E.coli BL21 cells (a kind gift from Monika Kudelska) for the expression of human tau40 isoform. Bacteria were grown at 37˚C in LB broth with 20μg/ml kanamycin until an optical density of 0.5-0.6 was reached at 600 nm absorbance. 1 mM Isopropyl beta-d-thiogalactopyranoside (IPTG, Sigma) was added to the bacterial culture to induce expression for 3.5 hours. Bacteria were then pelleted for 20 minutes at 5000 x g and stored at -20˚C overnight. Bacterial pellets were resuspended in homogenisation buffer (20 mM MES, 50 mM NaCl, 1mM $MgCl_2$, 1mM EGTA, 5 mM DTT, 1mM PMSF pH6.8) and sonicated for a total of 5 minutes (10 second pulses each separated by 45 seconds). Bacterial cell homogenate was then boiled at 95˚C for 20 minutes in order to denature globular proteins. Denatured proteins and cell debris were pelleted by centrifugation at 127,000 x g for 30 minutes at 4˚C. Supernatant was dialysed against buffer A (20 mM MES, 50 mM NaCl, 1mM $MgCl_2$, 1mM EGTA, 2 mM DTT, 0.1mM PMSF pH6.8) overnight (25 kDa cut-off, Spectra/Por). Samples were then loaded onto a cation exchange column and eluted against increasing concentrations of NaCl from buffer B (20 mM MES, 1 M NaCl, 2 mM DTT, 1mM $MgCl_2$, 1mM EGTA, 0.1mM PMSF pH6.8). Fractions were selected and combined based on SDS-PAGE, snap-frozen and stored at -20 ˚C for up to one week before use.

Protein Aggregation

BSA Fatty acid free BSA (Sigma, A7030) was dissolved directly into 10 mM HCl (pH2, ddH_2O) at a concentration of 60 mg/ml and filtered through a 0.22μm syringe filter. 1ml of the solution was heated in a 65˚C water bath to induce protein aggregation. 20μl of solution was removed at each time-point and added directly to ice to quench the reaction.

Tau Purified tau in elution buffer was exchanged into aggregation buffer (PBS; 10mM Na2HPO4, 2mM KH2PO4, 137 mM NaCl, 10mM KCl, 2mM DTT pH7.4) and by serial concentration and dilution through a 10 KDa MWCO filter (Vivaspin). Tau was concentrated to 3 mg/ml and heparin (sigma) was added at a 4:1 ratio, protein:heparin (mg/ml). Tau was then aggregated by incubation at 37˚C with shaking (220rpm). Fibrils were pelleted at 100,000 x G for 1 hour at 4 ˚C. Oligomers were first span at 100,000 x G for 1 hour at 4 ˚C to remove any pre-formed fibrils and then the supernatant was concentrated using a 100 kDa MWCO filter (Vivaspin).

β2M β2M was a kind gift from Eva Scherer. 6 mg/ml purified β2M in PBS was exchanged into aggregation buffer (50mM citrate, 100 mM NaCl, pH 2.5). PBS was removed by serial concentration and dilution through a 5 KDa MWCO filter (Vivaspin). β2M was diluted to 1 mg/ml and incubated at 37˚C with shaking (220rpm) for 24 hours (oligomers) and 14 days (fibrils). Fibrils were pelleted at 16,100 x G for 15 min at 4 ˚C. Oligomers were first span at 16,100 x G for 15 mins at 4 ˚C to remove any pre-formed fibrils and then the supernatant was concentrated using a 30 kDa MWCO filter (Vivaspin).

Raman spectroscopy and sample preparation

A Renishaw InVia microscope system was used for Raman spectroscopy. Quartz coverslips were coated in trichloro(1H,1H,2H,2H-perfluoroocytl)silane (Sigma) by chemical vapour deposition. A silane atmosphere was created by a 30 minute desiccation using a small volume of trichloro(1H,1H,2H,2H-perfluoroocytl)silane in a reaction chamber. Quartz coverslip surfaces were activated by oxygen plasma treatment before incubation in the silane atmosphere to create a silane monolayer on the coverslip surface for 2 hours. For Raman spectroscopy of wet protein samples, 10 µl of each protein sample was added to the quartz coverslip. For DDRS, 0.5 µl of each protein sample was first dried onto a quartz coverslip for 12 minutes under a vacuum. Spectra were then collected from the 'coffee ring' of each drop, where proteins are found in the absence of bulk salt.[17-18] The samples were excited using a 785 nm laser focused through a Leica 50x (0.75 NA) short working distance objective for DDRS and a 63x Leica water immersion (1.25 NA) objective for wet protein samples. Data was obtained and parameters were set using Renishaw WIRE4.1 software, WIRE was also used for cosmic ray removal. Spectra were collected in the fingerprint region (614 - 1722 cm^{-1}). The Raman system was calibrated to the 520 cm^{-1} reference peak of silicon prior to each experiment.

Spectral deconvolution

The spectra for each protein species were carefully background subtracted using blank/buffer spectra recorded on quartz. The Amide I region (1525 cm^{-1} – 1725 cm^{-1}) was then truncated using a linear baseline for background subtraction. The Amide I region was deconvolved using mixed Gaussian and Lorentzian using WIRE4.1 software. Four peaks, centred at 1550 cm^{-1}, 1580 cm^{-1}, 1606 cm^{-1} and 1616 cm^{-1}, were assigned to the aromatic amino acids tryptophan, phenylalanine and tryptophan. A further peak ~1635 cm^{-1} was assigned to nonregular structure/vibrational coupling and not included in secondary structural analysis. Three curves, representing secondary structural peaks, were centred near 1655 cm^{-1} (peak 1), 1670 cm^{-1} (peak 2) and 1686 cm^{-1} (peak 3). The starting curve frequency was determined by taking the second derivative of the Amide I region. Starting curve height was equal to the Amide I spectrum at that given frequency. All curves had starting bandwidths at half height (BWHH) of 15 cm^{-1}. Heterogeneous narrowing and broadening of curves was enabled to a maximum of 40 cm^{-1}. The percentage of secondary structure is determined by the dividing the area under the peak of interest by the sum of the area under peaks 1 to 3.

Principle Component Analysis

Principal Component Analysis (PCA) was performed using the IRootLab plugin (0.15.07.09-v) for MATLAB R2015a.[111] All spectra were carefully background subtracted using blank quartz spectra and a 5th order polynomial, and the ends of each spectra were anchored to the axis using the rubberband-like function**.** Spectra were smoothed using the wavelet denoising function before intensity normalization using the CH_2 band (~1450 cm^{-1}), or Amide I band. Trained-mean centering was then applied to the spectra before PCA with a maximum of ten principle components.

Atomic Force Microscopy

25 µl of ~0.3 – 0.6 mg/ml protein was added to a freshly cleaved 10 mm mica disc (Agar Scientific) and incubated at RT for 1 min (β2M), 2 min (BSA) and 15 min (Tau). The protein solution was then replaced with ddH_2O x3 before drying under a steady stream of nitrogen gas. Samples were imaged using a Digital Instruments Multimode IV AFM system operated in tapping mode. Aluminum coated, non-contact/Tapping mode probes with a resonance frequency of 320kHz and force constant of 42N/m were used for all images (Nanoworld, POINTPROBE NHCR). Probes were autotuned using Nanoscope III 5.12r3 software before use. Images shown are representative of the sample and were taken at random points on the sample with a scan rate of 1Hz-2Hz and 512 samples per line/512 lines per image. The samples were diluted 100x before drying on mica for AFM and species were allowed to bind to the surface for the same amount of time before a water washing step. Height analysis: height was measured across a lateral cross section in regions containing minimal overlap of features using WSxM Beta.[112]

Thioflavin T and Bis-ANS fluorescence

ThT and Bis-ANS (Sigma) were each separately dissolved in the equivalent buffer used for each protein. The fluorescent dyes were each mixed with protein samples to a final concentration of 10 µM dye and 10 µM protein. Solutions were transferred to 96-well plates (Costar) and fluorescence was measured using an excited filter of 450 nm and an emission filter of 490 nm. The fluorescence of each equivalent blank solution (buffer + dye) was subtracted from each protein and fluorescence was normalised as fold change over monomer.

ASSOCIATED CONTENT

Supporting Information: supplementary data with figures for AFM height profiles, Amide III and skeletal spectra, Deconvolution of wet Amide I spectra, Deconvolution of dried Amide I spectra, Fingerprint region for tau and heparin Raman spectra B AFM image of heparin bound to mica substrate using the same conditions as for tau/heparin imaging, Supplementary tables giving the PCA loadings of wet proteins and dried proteins and comparison across monomer, oligomers and fibrils.

The Supporting Information is available free of charge on the ACS Publications website.

AUTHOR INFORMATION

Corresponding Author

s.mahajan@soton.ac.uk; a.mudher@soton.ac.uk

Author contributions

SM and AM conceived the project. GD carried out all the experiments and the analysis. GD, SM and AM designed the experiments and analysed the results. WR and AC helped with the production of proteins and the biological assays. IN helped with the AFM and analysis of AFM results. GD, SM and AM wrote the manuscript. All authors contributed and approved the final manuscript.

ACKNOWLEDGMENT

Funding for this project is acknowledged from Rosetrees Trust (project M437). S.M. acknowledges support from ERC Grant NanoChemBioVision (638258). G. D. and A. M additionally acknowledges support from John and Elizabeth Bouldin. We acknowledge Eva Sherer for kindly providing purified β2M protein and Niall Hanrahan for his assistance in some experiments.

Notes

There are no conflicts to declare.

REFERENCES

1. Bayer, T. A., Proteinopathies, a core concept for understanding and ultimately treating degenerative disorders? *European Neuropsychopharmacology* **2015,** *25* (5), 713-724.
2. Breydo, L.; Uversky, V. N., Structural, morphological, and functional diversity of amyloid oligomers. *Febs Letters* **2015,** *589* (19), 2640-2648.
3. Cremades, N.; Cohen, S. I. A.; Deas, E.; Abramov, A. Y.; Chen, A. Y.; Orte, A.; Sandal, M.; Clarke, R. W.; Dunne, P.; Aprile, F. A.; Bertoncini, C. W.; Wood, N. W.; Knowles, T. P. J.; Dobson, C. M.; Klenerman, D., Direct Observation of the Interconversion of Normal and Toxic Forms of alpha-Synuclein. *Cell* **2012,** *149* (5), 1048-1059.
4. Kjaergaard, M.; Dear, A. J.; Kundel, F.; Qamar, S.; Meisl, G.; Knowles, T. P. J.; Klenerman, D., Oligomer Diversity during the Aggregation of the Repeat Region of Tau. *Acs Chem Neurosci* **2018,** *DOI: 10.1021/acschemneuro.8b00250 (PMID: 29953200).*
5. Capitini, C.; Patel, J. R.; Natalello, A.; D'Andrea, C.; Relini, A.; Jarvis, J. A.; Birolo, L.; Peduzzo, A.; Vendruscolo, M.; Matteini, P.; Dobson, C. M.; Simone, A.; Chiti, F., Structural differences between toxic and nontoxic HypF-N oligomers. *Chemical Communications* **2018,** *54* (62), 8637-8640.
6. Lasagna-Reeves, C. A.; Castillo-Carranza, D. L.; Guerrero-Munoz, M. J.; Jackson, G. R.; Kayed, R., Preparation and Characterization of Neurotoxic Tau Oligomers. *Biochemistry* **2010,** *49* (47), 10039-10041.
7. Lasagna-Reeves, C. A.; Castillo-Carranza, D. L.; Sengupta, U.; Clos, A. L.; Jackson, G. R.; Kayed, R., Tau oligomers impair memory and induce synaptic and mitochondrial dysfunction in wild-type mice. *Mol Neurodegener* **2011,** *6*.
8. Lasagna-Reeves, C. A.; Castillo-Carranza, D. L.; Sengupta, U.; Guerrero-Munoz, M. J.; Kiritoshi, T.; Neugebauer, V.; Jackson, G. R.; Kayed, R., Alzheimer brain-derived tau oligomers propagate pathology from endogenous tau. *Scientific Reports* **2012,** *2*.
9. Kayed, R.; Head, E.; Thompson, J. L.; McIntire, T. M.; Milton, S. C.; Cotman, C. W.; Glabe, C. G., Common structure of soluble amyloid oligomers implies common mechanism of pathogenesis. *Science* **2003,** *300* (5618), 486-489.
10. Bonhommeau, S.; Talaga, D.; Hunel, J.; Cullin, C.; Lecomte, S., Tip-Enhanced Raman Spectroscopy to Distinguish Toxic Oligomers from A beta(1-42) Fibrils at the Nanometer Scale. *Angew Chem Int Edit* **2017,** *56* (7), 1771-1774.
11. Campioni, S.; Mannini, B.; Zampagni, M.; Pensalfini, A.; Parrini, C.; Evangelisti, E.; Relini, A.; Stefani, M.; Dobson, C. M.; Cecchi, C.; Chiti, F., A causative link between the structure of aberrant protein oligomers and their toxicity. *Nat Chem Biol* **2010,** *6* (2), 140-147.
12. Bolognesi, B.; Kumita, J. R.; Barros, T. P.; Esbjorner, E. K.; Luheshi, L. M.; Crowther, D. C.; Wilson, M. R.; Dobson, C. M.; Favrin, G.; Yerbury, J. J., ANS Binding Reveals Common Features of Cytotoxic Amyloid Species. *Acs Chem Biol* **2010,** *5* (8), 735-740.
13. D'Andrea, C.; Foti, A.; Cottat, M.; Banchelli, M.; Capitini, C.; Barreca, F.; Canale, C.; de Angelis, M.; Relini, A.; Marago, O. M.; Pini, R.; Chiti, F.; Gucciardi, P. G.; Matteini, P., Nanoscale Discrimination between Toxic and Nontoxic Protein Misfolded Oligomers with Tip-Enhanced Raman Spectroscopy. *Small* **2018,** *14* (36).
14. Kurouski, D.; Van Duyne, R. P.; Lednev, I. K., Exploring the structure and formation mechanism of amyloid fibrils by Raman spectroscopy: a review. *Analyst* **2015,** *140* (15), 4967-4980.
15. Devitt, G.; Howard, K.; Mudher, A.; Mahajan, S., Raman Spectroscopy: An Emerging Tool in Neurodegenerative Disease Research and Diagnosis. *Acs Chem Neurosci* **2018,** *9* (3), 404-420.
16. Paraskevaidi, M.; Morais, C. L. M.; Halliwell, D. E.; Mann, D. M. A.; Allsop, D.; Martin-Hirsch, P. L.; Martin, F. L., Raman Spectroscopy to Diagnose Alzheimer's Disease and Dementia with Lewy Bodies in Blood. *Acs Chem Neurosci* **2018,** *9* (11), 2786-2794.
17. Zhang, D. M.; Mrozek, M. F.; Xie, Y.; Ben-Amotz, D., Chemical segregation and reduction of Raman background interference using drop coating deposition. *Applied Spectroscopy* **2004,** *58* (8), 929-933.
18. Ortiz, C.; Zhang, D. M.; Xie, Y.; Ribbe, A. E.; Ben-Amotz, D., Validation of the drop coating deposition Raman method for protein analysis. *Analytical Biochemistry* **2006,** *353* (2), 157-166.
19. Ashton, L.; Brewster, V. L.; Correa, E.; Goodacre, R., Detection of glycosylation and iron-binding protein modifications using Raman spectroscopy. *Analyst* **2017,** *142* (5), 808-814.
20. Zhang, D. M.; Ortiz, C.; Xie, Y.; Davisson, V. J.; Ben-Amotz, D., Detection of the site of phosphorylation in a peptide using Raman spectroscopy and partial least squares discriminant analysis. *Spectrochimica Acta Part a-Molecular and Biomolecular Spectroscopy* **2005,** *61* (3), 471-475.
21. Spiro, T. G.; Miskowsk.V; Tang, S. P. W.; Gaber, B. P.; Moss, T. H.; Shapiro, E. R., Resonance Raman-Spectroscopy as a Probe of Metal Binding-Sites - Transferrin and Blue Copper Proteins. *Abstr Pap Am Chem S* **1974**, 69-69.
22. Tomimats.Y; Scherer, J. R.; Kint, S., Laser Raman-Scattering of Protein Metal-Chelates. *Abstr Pap Am Chem S* **1974**, 169-169.
23. Maiti, N. C.; Apetri, M. M.; Zagorski, M. G.; Carey, P. R.; Anderson, V. E., Raman spectroscopic characterization of secondary structure in natively unfolded proteins: alpha-synuclein. *Journal of the American Chemical Society* **2004,** *126* (8), 2399-2408.
24. Flynn, J. D.; Lee, J. C., Raman fingerprints of amyloid structures. *Chemical Communications* **2018,** *54* (51), 6983-6986.
25. Apetri, M. M.; Maiti, N. C.; Zagorski, M. G.; Carey, P. R.; Anderson, V. E., Secondary structure of alpha-synuclein oligomers: Characterization by Raman and atomic force microscopy. *Journal of Molecular Biology* **2006,** *355* (1), 63-71.
26. Dalal, V.; Arya, S.; Bhattacharya, M.; Mukhopadhyay, S., Conformational Switching and Nanoscale Assembly of Human Prion Protein into Polymorphic Amyloids via Structurally Labile Oligomers. *Biochemistry* **2015,** *54* (51), 7505-7513.
27. Arya, S.; Kumari, A.; Dalal, V.; Bhattacharya, M.; Mukhopadhyay, S., Appearance of annular ring-like intermediates during amyloid fibril formation from human serum albumin. *Physical Chemistry Chemical Physics* **2015,** *17* (35), 22862-22871.
28. Roy, A.; Chandra, K.; Dolui, S.; Maiti, N. C., Envisaging the Structural Elevation in the Early Event of Oligomerization of Disordered Amyloid ss Peptide. *Acs Omega* **2017,** *2* (8), 4316-4327.
29. Flynn, J. D.; McGlinchey, R. P.; Walker, R. L.; Lee, J. C., Structural features of alpha-synuclein amyloid fibrils revealed by Raman spectroscopy. *Journal of Biological Chemistry* **2018,** *293* (3), 767-776.
30. Myshakina, N. S.; Ahmed, Z.; Asher, S. A., Dependence of amide vibrations on hydrogen bonding. *Journal of Physical Chemistry B* **2008,** *112* (38), 11873-11877.
31. Rygula, A.; Majzner, K.; Marzec, K. M.; Kaczor, A.; Pilarczyk, M.; Baranska, M., Raman spectroscopy of proteins: a review. *Journal of Raman Spectroscopy* **2013,** *44* (8), 1061-1076.

32. Signorelli, S.; Cannistraro, S.; Bizzarri, A. R., Structural Characterization of the Intrinsically Disordered Protein p53 Using Raman Spectroscopy. *Applied Spectroscopy* **2017,** *71* (5), 823-832.
33. Lippert, J. L.; Tyminski, D.; Desmeules, P. J., Determination of Secondary Structure of Proteins by Laser Raman-Spectroscopy. *Journal of the American Chemical Society* **1976,** *98* (22), 7075-7080.
34. Chen, M. C.; Lord, R. C., Laser-excited raman-spectroscopy of biomolecules .6. Some polypeptides as conformational models. *Journal of the American Chemical Society* **1974,** *96* (15), 4750-4752.
35. Lednev, I. K.; Karnoup, A. S.; Sparrow, M. C.; Asher, S. A., Nanosecond UV resonance Raman examination of initial steps in alpha-helix secondary structure evolution. *Journal of the American Chemical Society* **1999,** *121* (16), 4076-4077.
36. Lednev, I. K.; Karnoup, A. S.; Sparrow, M. C.; Asher, S. A., alpha-helix peptide folding and unfolding activation barriers: A nanosecond UV resonance raman study. *Journal of the American Chemical Society* **1999,** *121* (35), 8074-8086.
37. Barrett, T. W.; Peticolas, W. L.; Robson, R. M., Laser Raman Light-Scattering Observations of Conformational-Changes in Myosin Induced by Inorganic Salts. *Biophysical Journal* **1978,** *23* (3), 349-358.
38. Susi, H.; Byler, D. M., Fourier Deconvolution of the Amide-I Raman Band of Proteins as Related to Conformation. *Applied Spectroscopy* **1988,** *42* (5), 819-826.
39. **!!! INVALID CITATION !!! 29, 36-37**.
40. Foggia, M.; Taddei, P.; Torreggiani, A.; Dettin, M.; Tinti, A., *Self-assembling peptides for biomedical applications: IR and Raman spectroscopies for the study of secondary structure*. 2012; Vol. 2, p 231-272.
41. Merlot, A. M.; Kalinowski, D. S.; Richardson, D. R., Unraveling the mysteries of serum albumin-more than just a serum protein. *Frontiers in Physiology* **2014,** *5*.
42. Murayama, K.; Tomida, M., Heat-induced secondary structure and conformation change of bovine serum albumin investigated by Fourier transform infrared spectroscopy. *Biochemistry* **2004,** *43* (36), 11526-11532.
43. Holm, N. K.; Jespersen, S. K.; Thomassen, L. V.; Wolff, T. Y.; Sehgal, P.; Thomsen, L. A.; Christiansen, G.; Andersen, C. B.; Knudsen, A. D.; Otzen, D. E., Aggregation and fibrillation of bovine serum albumin. *Biochimica Et Biophysica Acta-Proteins and Proteomics* **2007,** *1774* (9), 1128-1138.
44. Usov, I.; Adamcik, J.; Mezzenga, R., Polymorphism in bovine serum albumin fibrils: morphology and statistical analysis. *Faraday Discussions* **2013,** *166*, 151-162.
45. Bhattacharya, M.; Jain, N.; Mukhopadhyay, S., Insights into the Mechanism of Aggregation and Fibril Formation from Bovine Serum Albumin. *Journal of Physical Chemistry B* **2011,** *115* (14), 4195-4205.
46. Majorek, K. A.; Porebski, P. J.; Dayal, A.; Zimmerman, M. D.; Jablonska, K.; Stewart, A. J.; Chruszcz, M.; Minor, W., Structural and immunologic characterization of bovine, horse, and rabbit serum albumins. *Molecular Immunology* **2012,** *52* (3-4), 174-182.
47. Shi, Z. S.; Olson, C. A.; Rose, G. D.; Baldwin, R. L.; Kallenbach, N. R., Polyproline II structure in a sequence of seven alanine residues. *Proceedings of the National Academy of Sciences of the United States of America* **2002,** *99* (14), 9190-9195.
48. Asher, S. A.; Mikhonin, A. V.; Bykov, S., UV Raman demonstrates that alpha-helical polyalanine peptides melt to polyproline II conformations. *Journal of the American Chemical Society* **2004,** *126* (27), 8433-8440.
49. Lagant, P.; Vergoten, G.; Fleury, G.; Loucheuxlefebvre, M. H., Raman-Spectroscopy and Normal Vibrations of Peptides - Characteristic Normal-Modes of a Type-Ii Beta-Turn. *European Journal of Biochemistry* **1984,** *139* (1), 137-148.
50. Mikhonin, A. V.; Ahmed, Z.; Ianoul, A.; Asher, S. A., Assignments and conformational dependencies of the amide III peptide backbone UV resonance Raman bands. *Journal of Physical Chemistry B* **2004,** *108* (49), 19020-19028.
51. Yu, T. J.; Lippert, J. L.; Peticola.Wl, Laser Raman Studies of Conformational Variations of Poly-L-Lysine. *Biopolymers* **1973,** *12* (9), 2161-2176.
52. Bailey, G. S.; Lee, J.; Tu, A. T., Conformational-Analysis of Myotoxin-Alpha (Muscle Degenerating Toxin) of Prairie Rattlesnake Venom - Predictions from Amino-Acid Sequence, Circular-Dichroism, and Raman-Spectroscopy. *Journal of Biological Chemistry* **1979,** *254* (18), 8922-8926.
53. Gazit, E., A possible role for pi-stacking in the self-assembly of amyloid fibrils. *Faseb Journal* **2002,** *16* (1), 77-83.
54. Sogawa, K.; Minoura, K.; In, Y.; Ishida, T.; Taniguchi, T.; Tomoo, K., CH-pi Interaction in VQIVYK Sequence Elucidated by NMR Spectroscopy is Essential for PHF Formation of Tau. *Biopolymers* **2014,** *102* (3), 288-295.
55. Makwana, K. M.; Mahalakshmi, R., Implications of aromatic-aromatic interactions: From protein structures to peptide models. *Protein Science* **2015,** *24* (12), 1920-1933.
56. Drueke, T. B., beta(2)-Microglobulin and amyloidosis. *Nephrol Dial Transpl* **2000,** *15*, 17-24.
57. Bjorkman, P. J.; Saper, M. A.; Samraoui, B.; Bennett, W. S.; Strominger, J. L.; Wiley, D. C., Structure of the Human Class-I Histocompatibility Antigen, Hla-A2. *Nature* **1987,** *329* (6139), 506-512.
58. Becker, J. W.; Reeke, G. N., 3-Dimensional Structure of Beta-2-Microglobulin. *Proceedings of the National Academy of Sciences of the United States of America* **1985,** *82* (12), 4225-4229.
59. Hiramatsu, H.; Lu, M.; Matsuo, K.; Gekko, K.; Goto, Y. J.; Kitagawa, T., Differences in the Molecular Structure of beta(2)-Microglobulin between Two Morphologically Different Amyloid Fibrils. *Biochemistry* **2010,** *49* (4), 742-751.
60. Vass, E.; Hollosi, M.; Besson, F.; Buchet, R., Vibrational spectroscopic detection of beta- and gamma-turns in synthetic and natural peptides and proteins. *Chem Rev* **2003,** *103* (5), 1917-1954.
61. Huang, C. Y.; Balakrishnan, G.; Spiro, T. G., Protein secondary structure from deep-UV resonance Raman spectroscopy. *Journal of Raman Spectroscopy* **2006,** *37* (1-3), 277-282.
62. Pande, J.; Pande, C.; Gilg, D.; Vasak, M.; Callender, R.; Kagi, J. H. R., Raman, Infrared, and Circular-Dichroism Spectroscopic Studies on Metallothionein - a Predominantly Turn-Containing Protein. *Biochemistry* **1986,** *25* (19), 5526-5532.
63. Ishizaki, H.; Balaram, P.; Nagaraj, R.; Venkatachalapathi, Y. V.; Tu, A. T., Determination of Beta-Turn Conformation by Laser Raman-Spectroscopy. *Biophysical Journal* **1981,** *36* (3), 509-517.
64. Cleveland, D. W.; Hwo, S. Y.; Weingarten, M. D.; Witman, G. B.; Kirschner, M. W., Mechanism of action of tau protein in microtubule assembly. *Journal of Cell Biology* **1975,** *67* (2), A72-A72.
65. Williams, D. R., Tauopathies: classification and clinical update on neurodegenerative diseases associated with microtubule-associated protein tau. *Intern Med J* **2006,** *36* (10), 652-660.
66. Fitzpatrick, A. W. P.; Falcon, B.; He, S.; Murzin, A. G.; Murshudov, G.; Garringer, H. J.; Crowther, R. A.; Ghetti, B.; Goedert, M.; Scheres, S. H. W., Cryo-EM structures of tau filaments from Alzheimer's disease. *Nature* **2017,** *547* (7662), 185-+.
67. Falcon, B.; Zhang, W. J.; Murzin, A. G.; Murshudov, G.; Garringer, H. J.; Vidal, R.; Crowther, R. A.; Ghetti, B.; Scheres, S. H. W.; Goedert, M., Structures of filaments from Pick's disease reveal a novel tau protein fold. *Nature* **2018,** *561* (7721), 137-+.
68. Goedert, M.; Jakes, R.; Spillantini, M. G.; Hasegawa, M.; Smith, M. J.; Crowther, R. A., Assembly of microtubule-associated protein tau into Alzheimer-like filaments induced by sulphated glycosaminoglycans. *Nature* **1996,** *383* (6600), 550-553.
69. Kaniyappan, S.; Chandupatla, R. R.; Mandelkow, E. M.; Mandelkow, E., Extracellular low-n oligomers of tau cause selective synaptotoxicity without affecting cell viability. *Alzheimers & Dementia* **2017,** *13* (11), 1270-1291.
70. Yoneda, J. S.; Miles, A. J.; Araujo, A. P. U.; Wallace, B. A., Differential dehydration effects on globular proteins and intrinsically disordered proteins during film formation. *Protein Science* **2017,** *26* (4), 718-726.
71. Frushour, B. G.; Koenig, J. L., Raman Studies of Crystalline, Solution, and Alkaline-Denatured States of Beta-Lactoglobulin. *Biopolymers* **1975,** *14* (3), 649-662.
72. Berriman, J.; Serpell, L. C.; Oberg, K. A.; Fink, A. L.; Goedert, M.; Crowther, R. A., Tau filaments from human brain and from in vitro assembly of recombinant protein show cross-beta structure. *Proceedings of the National Academy of Sciences of the United States of America* **2003,** *100* (15), 9034-9038.
73. Kirschner, D. A.; Abraham, C.; Selkoe, D. J., X-ray-diffraction from intraneuronal paired helical filaments and extraneuronal amyloid fibers in alzheimer-disease indicates cross-beta conformation. *Proceedings of the National Academy of Sciences of the United States of America* **1986,** *83* (2), 503-507.
74. Frost, B.; Ollesch, J.; Wille, H.; Diamond, M. I., Conformational Diversity of Wild-type Tau Fibrils Specified by Templated Conformation Change. *Journal of Biological Chemistry* **2009,** *284* (6), 3546-3551.

75. Schweers, O.; Schonbrunnhanebeck, E.; Marx, A.; Mandelkow, E., Structural studies of tau-protein and alzheimer paired helical filaments show no evidence for beta-structure. *Journal of Biological Chemistry* **1994,** *269* (39), 24290-24297.
76. Na, J. H.; Lee, W. K.; Yu, Y. G., How Do We Study the Dynamic Structure of Unstructured Proteins: A Case Study on Nopp140 as an Example of a Large, Intrinsically Disordered Protein. *Int J Mol Sci* **2018,** *19* (2).
77. McParland, V. J.; Kad, N. M.; Kalverda, A. P.; Brown, A.; Kirwin-Jones, P.; Hunter, M. G.; Sunde, M.; Radford, S. E., Partially unfolded states of beta(2)-microglobulin and amyloid formation in vitro. *Biochemistry* **2000,** *39* (30), 8735-8746.
78. Uversky, V. N.; Li, J.; Fink, A. L., Evidence for a partially folded intermediate in alpha-synuclein fibril formation. *Journal of Biological Chemistry* **2001,** *276* (14), 10737-10744.
79. Wang, Y. T.; Petty, S.; Trojanowski, A.; Knee, K.; Goulet, D.; Mukerji, I.; King, J., Formation of Amyloid Fibrils In Vitro from Partially Unfolded Intermediates of Human gamma C-Crystallin. *Invest Ophth Vis Sci* **2010,** *51* (2), 672-678.
80. Armen, R. S.; Daggett, V., Characterization of two distinct beta(2)-microglobulin unfolding intermediates that may lead to amyloid fibrils of different morphology. *Biochemistry* **2005,** *44* (49), 16098-16107.
81. Calamai, M.; Chiti, F.; Dobson, C. M., Amyloid fibril formation can proceed from different conformations of a partially unfolded protein. *Biophysical Journal* **2005,** *89* (6), 4201-4210.
82. Khurana, R.; Gillespie, J. R.; Talapatra, A.; Minert, L. J.; Ionescu-Zanetti, C.; Millett, I.; Fink, A. L., Partially folded intermediates as critical precursors of light chain amyloid fibrils and amorphous aggregates. *Biochemistry* **2001,** *40* (12), 3525-3535.
83. Filik, J.; Stone, N., Investigation into the protein composition of human tear fluid using centrifugal filters and drop coating deposition Raman spectroscopy. *Journal of Raman Spectroscopy* **2009,** *40* (2), 218-224.
84. Filik, J.; Stone, N., Drop coating deposition Raman spectroscopy of protein mixtures. *Analyst* **2007,** *132* (6), 544-550.
85. Meyer, V.; Holden, M. R.; Weismiller, H. A.; Eaton, G. R.; Eaton, S. S.; Margittai, M., Fracture and Growth Are Competing Forces Determining the Fate of Conformers in Tau Fibril Populations. *Journal of Biological Chemistry* **2016,** *291* (23), 12271-12281.
86. Surmacz-Chwedoruk, W.; Babenko, V.; Dec, R.; Szymczak, P.; Dzwolak, W., The emergence of superstructural order in insulin amyloid fibrils upon multiple rounds of self-seeding. *Scientific Reports* **2016,** *6*.
87. Ramachandran, G.; Milan-Garces, E. A.; Udgaonkar, J. B.; Puranik, M., Resonance Raman Spectroscopic Measurements Delineate the Structural Changes that Occur during Tau Fibril Formation. *Biochemistry* **2014,** *53* (41), 6550-6565.
88. Clavaguera, F.; Akatsu, H.; Fraser, G.; Crowther, R. A.; Frank, S.; Hench, J.; Probst, A.; Winkler, D. T.; Reichwald, J.; Staufenbiel, M.; Ghetti, B.; Goedert, M.; Tolnay, M., Brain homogenates from human tauopathies induce tau inclusions in mouse brain. *Proceedings of the National Academy of Sciences of the United States of America* **2013,** *110* (23), 9535-9540.
89. Narasimhan, S.; Guo, J. L.; Changolkar, L.; Stieber, A.; McBride, J. D.; Silva, L. V.; He, Z. H.; Zhang, B.; Gathagan, R. J.; Trojanowski, J. Q.; Lee, V. M. Y., Pathological Tau Strains from Human Brains Recapitulate the Diversity of Tauopathies in Nontransgenic Mouse Brain. *Journal of Neuroscience* **2017,** *37* (47), 11406-11423.
90. Kaufman, S. K.; Thomas, T. L.; Del Tredici, K.; Braak, H.; Diamond, M. I., Characterization of tau prion seeding activity and strains from formaldehyde-fixed tissue. *Acta Neuropathol Com* **2017,** *5*.
91. Sanders, D. W.; Kaufman, S. K.; DeVos, S. L.; Sharma, A. M.; Mirbaha, H.; Li, A. M.; Barker, S. J.; Foley, A. C.; Thorpe, J. R.; Serpell, L. C.; Miller, T. M.; Grinberg, L. T.; Seeley, W. W.; Diamond, M. I., Distinct Tau Prion Strains Propagate in Cells and Mice and Define Different Tauopathies. *Neuron* **2014,** *82* (6), 1271-1288.
92. Bousset, L.; Pieri, L.; Ruiz-Arlandis, G.; Gath, J.; Jensen, P. H.; Habenstein, B.; Madiona, K.; Olieric, V.; Bockmann, A.; Meier, B. H.; Melki, R., Structural and functional characterization of two alpha-synuclein strains. *Nature Communications* **2013,** *4*.
93. Peelaerts, W.; Bousset, L.; Van der Perren, A.; Moskalyuk, A.; Pulizzi, R.; Giugliano, M.; Van den Haute, C.; Melki, R.; Baekelandt, V., alpha-Synuclein strains cause distinct synucleinopathies after local and systemic administration. *Nature* **2015,** *522* (7556), 340-+.
94. Peng, C.; Gathagan, R. J.; Lee, V. M. Y., Distinct alpha-Synuclein strains and implications for heterogeneity among alpha-Synucleinopathies. *Neurobiol Dis* **2018,** *109*, 209-218.
95. Guo, J. L.; Covell, D. J.; Daniels, J. P.; Iba, M.; Stieber, A.; Zhang, B.; Riddle, D. M.; Kwong, L. K.; Xu, Y.; Trojanowski, J. Q.; Lee, V. M. Y., Distinct alpha-Synuclein Strains Differentially Promote Tau Inclusions in Neurons. *Cell* **2013,** *154* (1), 103-117.
96. Prusiner, S. B.; Woerman, A. L.; Mordes, D. A.; Watts, J. C.; Rampersaud, R.; Berry, D. B.; Patel, S.; Oehler, A.; Lowe, J. K.; Kravitz, S. N.; Geschwind, D. H.; Glidden, D. V.; Halliday, G. M.; Middleton, L. T.; Gentleman, S. M.; Grinberg, L. T.; Giles, K., Evidence for alpha-synuclein prions causing multiple system atrophy in humans with parkinsonism. *Proceedings of the National Academy of Sciences of the United States of America* **2015,** *112* (38), E5308-E5317.
97. Woerman, A. L.; Stohr, J.; Aoyagi, A.; Rampersaud, R.; Krejciova, Z.; Watts, J. C.; Ohyama, T.; Patel, S.; Widjaja, K.; Oehler, A.; Sanders, D. W.; Diamond, M. I.; Seeley, W. W.; Middleton, L. T.; Gentleman, S. M.; Mordes, D. A.; Sudhof, T. C.; Giles, K.; Prusiner, S. B., Propagation of prions causing synucleinopathies in cultured cells. *Proceedings of the National Academy of Sciences of the United States of America* **2015,** *112* (35), E4949-E4958.
98. Guo, J. L.; Lee, V. M. Y., Seeding of Normal Tau by Pathological Tau Conformers Drives Pathogenesis of Alzheimer-like Tangles. *Journal of Biological Chemistry* **2011,** *286* (17), 15317-15331.
99. Gould, N.; Mor, D. E.; Lightfoot, R.; Malkus, K.; Giasson, B.; Ischiropoulos, H., Evidence of Native alpha-Synuclein Conformers in the Human Brain. *Journal of Biological Chemistry* **2014,** *289* (11), 7929-7934.
100. Guo, J. L.; Narasimhan, S.; Changolkar, L.; He, Z. H.; Stieber, A.; Zhang, B.; Gathagan, R. J.; Iba, M.; McBride, J. D.; Trojanowski, J. Q.; Lee, V. M. Y., Unique pathological tau conformers from Alzheimer's brains transmit tau pathology in nontransgenic mice. *J Exp Med* **2016,** *213* (12), 2635-2654.
101. Jung, B. C.; Lim, Y. J.; Bae, E. J.; Lee, J. S.; Choi, M. S.; Lee, M. K.; Lee, H. J.; Kim, Y. S.; Lee, S. J., Amplification of distinct alpha-synuclein fibril conformers through protein misfolding cyclic amplification. *Exp Mol Med* **2017,** *49*.
102. Gibbons, G. S.; Banks, R. A.; Kim, B.; Changolkar, L.; Riddle, D. M.; Leight, S. N.; Irwin, D. J.; Trojanowski, J. Q.; Lee, V. M. Y., Detection of Alzheimer Disease (AD)-Specific Tau Pathology in AD and NonAD Tauopathies by Immunohistochemistry With Novel Conformation-Selective Tau Antibodies. *Journal of Neuropathology and Experimental Neurology* **2018,** *77* (3), 216-228.
103. Kayed, R.; Canto, I.; Breydo, L.; Rasool, S.; Lukacsovich, T.; Wu, J.; Albay, R.; Pensalfini, A.; Yeung, S.; Head, E.; Marsh, J. L.; Glabe, C., Conformation dependent monoclonal antibodies distinguish different replicating strains or conformers of prefibrillar A beta oligomers. *Mol Neurodegener* **2010,** *5*.
104. Bittar, A.; Sengupta, U.; Kayed, R., Prospects for strain-specific immunotherapy in Alzheimer's disease and tauopathies. *Npj Vaccines* **2018,** *3*.
105. Shashilov, V.; Xu, M.; Makarava, N.; Savtchenko, R.; Baskakov, I. V.; Lednev, I. K., Dissecting Structure of Prion Amyloid Fibrils by Hydrogen-Deuterium Exchange Ultraviolet Raman Spectroscopy. *Journal of Physical Chemistry B* **2012,** *116* (27), 7926-7930.
106. Jermyn, M.; Mok, K.; Mercier, J.; Desroches, J.; Pichette, J.; Saint-Arnaud, K.; Bernstein, L.; Guiot, M. C.; Petrecca, K.; Leblond, F., Intraoperative brain cancer detection with Raman spectroscopy in humans. *Science Translational Medicine* **2015,** *7* (274).
107. Paraskevaidi, M.; Morais, C. L. M.; Lima, K. M. G.; Snowden, J. S.; Saxon, J. A.; Richardson, A. M. T.; Jones, M.; Mann, D. M. A.; Allsop, D.; Martin-Hirsch, P. L.; Martin, F. L., Differential diagnosis of Alzheimer's disease using spectrochemical analysis of blood. *Proceedings of the National Academy of Sciences of the United States of America* **2017,** *114* (38), E7929-E7938.
108. Villa-Manriquez, J. F.; Castro-Ramos, J.; Gutierrez-Delgado, F.; Lopez-Pacheco, M. A.; Villanueva-Luna, A. E., Raman spectroscopy and PCA-SVM as a non-invasive diagnostic tool to identify and classify qualitatively glycated hemoglobin levels in vivo. *Journal of Biophotonics* **2017,** *10* (8), 1074-1079.
109. Liu, W. J.; Sun, Z. T.; Chen, J. Y.; Jing, C. B., Raman Spectroscopy in Colorectal Cancer Diagnostics: Comparison of PCA-LDA and PLS-DA Models. *J Spectrosc* **2016**.
110. Li, X. Z.; Yang, T. Y.; Li, S. Q.; Wang, D. L.; Song, Y. T.; Zhang, S., Raman spectroscopy combined with principal component

analysis and k nearest neighbour analysis for non-invasive detection of colon cancer. *Laser Physics* **2016,** *26* (3).
111. Trevisan, J.; Angelov, P. P.; Scott, A. D.; Carmichael, P. L.; Martin, F. L., IRootLab: a free and open-source MATLAB toolbox for vibrational biospectroscopy data analysis. *Bioinformatics* **2013,** *29* (8), 1095-1097.
112. Horcas, I.; Fernandez, R.; Gomez-Rodriguez, J. M.; Colchero, J.; Gomez-Herrero, J.; Baro, A. M., WSXM: A software for scanning probe microscopy and a tool for nanotechnology. *Rev Sci Instrum* **2007,** *78* (1).

Table of Contents (TOC)